Spring 2008

Frontal Variability in Drake Passage - A Modeling Study

Bin Zhang
Old Dominion University

FRONTAL VARIABILITY IN DRAKE PASSAGE

- A MODELING STUDY

by

Bin Zhang
B.S. 1996, University of Science and Technology of China
M.S. 1999, Institute of Oceanology of Chinese Academy of Sciences

A Dissertation Submitted to the Faculty of
Old Dominion University in Partial Fulfillment of the
Requirement for the Degree of

DOCTOR OF PHILOSOPHY

OCEANOGRAPHY

OLD DOMINION UNIVERSITY
May 2008

Approved by:

John M. Klinck (Director)

Arnoldo Valle-Levinson (Member)

Chester E. Grosch (Member)

John A. Adam (Member)

Thomas C. Rover (Member)

Sarah T. Gille (Member)

ABSTRACT

FRONTAL VARIABILITY IN DRAKE PASSAGE - A MODELING STUDY

Bin Zhang
Old Dominion University, 2008
Director: Dr. John M. Klinck

The Antarctic Circumpolar Current (ACC) features three major fronts: the Subantarctic Front (SAF), the Polar Front (PF), the Southern ACC Front (SACCF). The locations of these fronts are not stable. The PF can shift away from its historical mean locations on the order of 100 km. The ACC transport in Drake Passage varies over a large range (50 to 60 Sv). Numerical simulations with the Regional Ocean Modeling System are carried out to study the frontal variability under the influence of ACC transport, local wind stress and bottom topography in Drake Passage.

Front-embedded numerical experiments are carried out without surface forcing for different ACC transports (from 95 to 155 Sv with an interval of 10 Sv). Large transport shifts the fronts northward while the fronts move southward with small transport. The mean shifting distance of the PF from the historical mean location is minimum with 135 Sv transport. The SAF and the SACC are confined by northern and southern continents, respectively, while the PF is loosely controlled by the topography. Due to impact of the eddies and meanders on the PF at several regions in Drake Passage, the PF may move northward to join the SAF or move southward to combine with the SACCF, especially in the central Scotia Sea. The SAF and PF are more stable with higher transport. The SAF behaves as a narrow, strong frontal jet with large transport while displaying wavy structure with smaller transport. In the model, the relationship between Ertel Potential Vorticity (EPV) and the 2D stream function is examined at different depth. The linear correlation coefficient between the EPV and the stream function is more than 0.9 between 1000 meter and 2500 meter depth while in the upper 500 meters it is less than 0.3, and near the bottom it is around 0.6. The smaller coefficient is caused by the removal of potential vorticity by friction and strong mixing.

Similiar simulations with 135 Sv transport but with different wind stress applied

on the surface are carried out to study the local wind stress effects. Three kinds of surface wind stress are the 6 hourly QSCAT/NCEP blended wind stress, monthly running mean filtered wind stress and zero wind stress. With 6 hourly wind stress, the PF location is more variable than that with the monthly running mean filtered wind stress.

The mean PF location changes with different wind stress. This change is different at different locations in the model. The surface elevation to each side of PF changes with the wind forcing. The peak frequencies at which the wind stress is correlated to the surface elevation above the 95% confidence level in the south are the 8 and 30 days with the wind stress change leading the surface elevation change. The peak frequencies to the north of the PF are 8, 15 and 40 days. The positive phase lag at some frequencies might be due to the contamination from the local baroclinic instabilities.

The mean 500 m temperature tracked PF location is consisitent with mean surface PF location. The surface PF tends to be south of the 500 m PF front. This difference between the surface and 500 m PF locations is modulated by the wind stress and the topography. With stronger wind stress, the difference is reduced.

Form drag from large variation of bottom topography shows little change with different wind stress in the model. The form drag in Drake Passage is calculated to be one order of magnitude larger than the local wind stress. The bottom skin stress can be neglected compared to other terms. Form drag is primarily due to remote forcing (the transport variations) instead of the influence of the local wind stress.

ACKNOWLEDGEMENTS

Writing a dissertation could take just weeks or months, while it is at the end of more than 20 years of school study. In this long journey, I could not finish without support from so many people. My sincere gratitude goes to my wife, parents, sisters and uncle.

I wish to thank Dr. John Klinck for his support and help during these years, for his inspiring, patience and efforts in guiding numerous computational experiments and editing manuscripts.

I wish to thank Dr. Tom Royer for his support and encouragement in the program, and for his reviewing and advice in this research. I wish to thank Dr. Eileen Hofmann for the discussion and suggestions in the research.

I would like to thank Dr. Sarah Gille, Dr. Arnoldo Valle-Levinson, Dr. Chet Grosch and Dr. John Adam for their reviewing, suggestions and comments on the manuscript.

I would also like to thank all the CCPO faculty and staff members for their support, help and active classes. Thanks to all graduate students here at CCPO for the friendship and good time.

TABLE OF CONTENTS

LIST OF TABLES

LIST OF FIGURES

CHAPTER I

INTRODUCTION

I.1 INTRODUCTION

The Southern Ocean is a truly global ocean that connects all the large oceans in the world[1]. It plays an important role in the global heat exchange between the ocean and the atmosphere and in the world ocean thermohaline circulation. The continuous zonal current in the Southern Ocean is the pathway that transports the upwelled North Atlantic Deep Water into the other parts of the world ocean, and releases heat into the atmosphere at the same time. The upwelling of Deep Water tilts the pycnocline to the surface at high southern latitudes causing the Antarctic Circumpolar Current (ACC) to have a large geostrophic transport. The sinking of the cold saline surface water along the continental slope, the upwelling of the Deep Water above Bottom Water and the northward subduction of the cold fresher water delineate the Southern Ocean as being composed of many regions with different water masses.

The frontal jets embedded in the ACC are unstable. The instabilities release potential energy and transfer salt and heat across fronts. Frontal locations change because of developing instabilities and also in response to the constantly changing local and global forcing. Although the ACC flow is zonal, characterized by mostly zonally uniform properties, the frontal variability is not zonal. Local frontal variability is controlled by many factors, such as local wind stress, the ACC transport and local bathymetry.

Drake Passage connects the Pacific Ocean and the Atlantic Ocean. It opens for exchange of volume, heat and salt between the two oceans and plays an important role in the world ocean circulation system. At the same time, it is a choke point of the ACC. The ACC enters into Drake Passage encountering with barriers by bathymetry shoaling and lateral constraints by the northern and southern walls. In Drake Passage, the ACC becomes stronger, narrower and swift and dynamics becomes complicated. Adjacent fronts become close each other and possibly merge together. While the

[1]This dissertation follows the citation style of Journal of Geophysical Research

transport and basic structure of the ACC are kept, local hydrography and frontal variability are different from those at other places.

The present study is to simulate the ACC fronts in Drake Passage with a regional ocean modeling system. The purpose of this study is to describe the frontal variability, explore the dynamical causes of the variability and understand the interaction of the fronts and topography in order to illustrate the importance of Drake Passage in the dynamics of the ACC.

I.1.1 Review of Antarctic Circumpolar Current

The ACC is unique in many aspects. The strongest winds blow over the Southern Ocean as westerlies. The strong zonal wind drives the ACC unhindered by the meridional continental boundaries and so the circulation is similar to the situation in the atmosphere. The mean transport of the ACC through Drake Passage is estimated to be 134 Sv [*Whitworth*, 1983], and net baroclinic transport has been steady for 20 years [*Cunningham et al.*, 2003]. The ACC is not restricted to the upper few hundred meters of the ocean but extends to great depth, and the average speed is about 1~4 cm/s eastward at 2500 m depth [*Tomczak and Godfrey*, 2003]. Therefore, the ACC has the largest mass transport of all ocean currents.

The dynamics of the ACC have been much debated for more than half a century. There is still much debate on the mechanisms controlling the transport of the ACC. *Munk and Palmen* [1951] suggested the transport of the ACC is directly proportional to the wind stress. *Stommel* [1957] proposed that the ACC is just like the subtropical gyre, which gains vorticity from the wind stress curl on the way circling the Antarctic while releasing the vorticity in Drake Passage as a return circulation; so, the wind stress curl should determine the ACC transport. *Nowlin and Klinck* [1986] found the ACC dynamics involve wind stress, form drag, lateral friction and Coriolis force; but the main balance is the wind stress and the form drag due to topography. *Warren et al.* [1996] examined the vertically integrated zonal momentum equation along the parallel latitudes that define the Drake Passage zone, and proposed that form drag has little relation to the transport of the ACC and revised the Sverdrup balance proposed by Stommel. Warren et al.'s paper has encouraged much debate. Following Warren et al., however, *Hughes* [1997] responded that the concept of form drag is

one of several important considerations in understanding the ACC dynamics and is the one that most clearly distinguishes the ACC from mid ocean gyres. *Tansley and Marshall* [2001] concluded from a simple channel model that the Sverdrup balance did not determine the transport of the ACC.

Gnanadesikan and Hallberg [2000] considered the thermodynamics in the Southern Ocean and pointed out the thermohaline balance is also important for the balance of forces acting on the ACC. The buoyancy forcing can determine the way that the wind stress balances the pressure gradient. By analyzing results of a circulation model coupled with a sea ice model, *Gent et al.* [2001] found that the ACC transport at the latitude of Drake Passage is related to the thermohaline overturning along the Antarctic Continental Shelf.

Adjacent to the continental area, buoyancy forcing due to melting of ice and the polar easterlies drives the westward current along the continental boundary except in some areas such as the shelf along the west Antarctic Peninsula. The easterly current varies seasonally since the melting of ice in summer increases the buoyancy forcing while in winter the injection of brine increases the vertical mixing.

The ACC is zonally continuous, consisting of three meridionally distributed jets. Each jet is associated with one front. From north to south they are the Subantarctic Front (SAF), the Polar Front (PF) and the Southern ACC Front (SACCF). Between adjacent fronts are zones with nearly homogeneous water mass properties [*Whitworth*, 1980; *Nowlin and Clifford*, 1982; *Nowlin and Klinck*, 1986; *Orsi et al.*, 1995]. *Hofmann* [1985] analyzed the distribution of FGGE drifters obtaining an average speed in each frontal jet and frontal zone. The distribution of drifters showed the meridional zonation of the ACC. *Gille* [1994] mapped the frontal jets, associated with changes in sea surface elevation, finding an average width of about 44 km for both the SAF and the PF. The average height difference across the SAF and PF are 0.7 m and 0.6 m, respectively. A temperature gradient of $1.35°C$ across the PF with a 45 km width seems to be the best surface expression of the PF [*Moore et al.*, 1997].

The fronts in the Southern Ocean shift with different spatial and temporal scales. Year-long current meter observations showed shifting and meandering of the fronts, ring development and their interaction with topography [*Hofmann and Whitworth*, 1985]. Geosat data indicate a decorrelation scale of 85 km and a temporal e-folding

scale of 34 days [*Gille and Kelly*, 1996]. There is an inverse relationship between the frontal meandering intensity and the underlying topography [*Moore et al.*, 1999]. Observations show that near large bathymetry features (large gradient of planetary potential vorticity), the PF becomes intensified and the meandering is inhibited.

In summary, the ACC is vigorous in kinetics and complicated in dynamics. It displays a general zonal banded structure but also shows variations.

Observations in the Southern Ocean are more difficult than in other parts of the world ocean due to the remote location and poor weather conditions. Therefore, numerical models are important in understanding the dynamics of the the ACC. Quasi-geostrophic models have long been used to investigate the large scale and mesoscale dynamics of the ACC [*Nowlin and Klinck*, 1986]. These models effectively detect the correlation among the wind stress (and stress curl), topography, Coriolis acceleration and eddy viscosity.

Primitive equation models are also used today due to improvement of computational capacity. The Fine Resolution Antarctic Model (FRAM) [*Webb et al.*, 1991] gives a good simulation of the ACC by restoring Levitus climatological data on the surface. Mesoscale jet structures are permitted in FRAM [*Sinha and Richards*, 1999], but the grid spacing is not small enough to resolve the ACC frontal variability. Another primitive equation model which also gives the ACC simulation is the Parallel Ocean Program (POP) [*Dukowicz and Smith*, 1994]. Many comparisons have been made regarding the results of these two models [*Sinha and Richards*, 1999; *Best et al.*, 1999]. POP model grid spacing is less than FRAM grid spacing, yet these two models only marginally resolve eddies, because their horizontal resolution is still not high enough [*Best et al.*, 1999]. Ongoing projects using global circulation models with very high resolution may give a new view of the frontal structure, such as the "Development of Super High Resolution Atmospheric and Oceanic General Circulation Models on Quasi-Uniform Grids" [*Tanaka*, 2004] in Japan.

I.1.2 Drake Passage observations and models

Many observations have been made in Drake Passage to quantify the transport of the ACC, the zonation of the ACC as well as the vertical structure of hydrography. The International Southern Ocean Studies (ISOS), a series of experiments from 1975 to 1980, mainly focused on Drake Passage. The most abundant data are from DRAKE79 (Jan, 1979 to Feb, 1980); numerous papers resulted from the data analysis. Since the middle 1980s, the World Ocean Circulation Experiment (WOCE) cruises and the available satellite sea surface height and the sea surface temperature data prompted further study of circulation and hydrology in Drake Passage as well as the whole Southern Ocean. From early 1990s, Long Term Ecological Research program at Palmer Station, studying ecological processes, have enhanced the understanding of the Drake Passage circulation. Some research has been focused on the Western Antarctic Peninsula (WAP) shelf to determine the water exchange between the shelf and the ACC [*Dinniman and Klinck*, 2004]. The Southern Ocean GLOBEC program, started in 2001, also focused on this area. A number of international collaborative studies are ongoing for different regions in the Southern Ocean as well as in Drake Passage.

From hydrography observations, the water masses in Drake Passage can be divided into seven groups [*Sievers and Nowlin*, 1984] (Fig. 1). Surface waters are the Antarctic Surface Water (AASW) south of the PF and the Subantarctic Surface Water (SASW), which undergo large seasonal changes as a result of heat exchange and ice formation. The homogeneous Subantarctic Mode Water (SAMW) in the Subantarctic Zone, is characterized by a weak vertical gradient and a weak maxima in salinity and oxygen. Just below the SAMW is the Antarctic Intermediate Water (AAIW), characterized by its salinity minimum and oxygen maximum. The Circumpolar Deep Water (CDW) originates from the North Atlantic Deep Water, fills most of the passage, joins the ACC and upwells. Below the CDW, south of the PF is a small portion of the South Pacific Deep Water, characterized by a maximum in silicate concentration. The densest water mass is the Weddell Sea Deep Water (WSDW) located on the bottom, intruding westward through the gap in the Scotia Ridge. *Well et al.* [2003] revealed an additional water mass, the South Pacific Deep Slope Water (SPDSW), with densities intermediate between the Upper CDW (UCDW) and Lower CDW (LCDW).

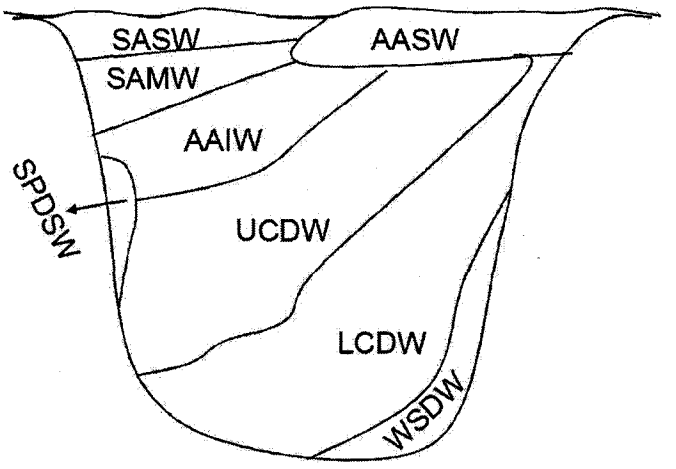

FIG. 1: Schematic plot of water masses in Drake Passage. AASW represents the Antarctic Surface Water. SASW represents the Subantarctic Surface Water. SAMW represents the Subantarctic Mode Water. AAIW represents the Antarctic Intermediate Water. UCDW represents the Upper Circumpolar Deep Water. LCDW represents the Lower Circumpolar Deep Water. WSDW represents the Weddell Sea Deep Water. SPDSW represents the South Pacific Deep Slope Water.

In spite of the intrusion of the environmental water masses, the transport of the ACC can still be better estimated in Drake Passage than in other regions. From the ISOS experiments, the time-averaged ACC transport is estimated as 134 Sv with not more than 10% uncertainty and with a range of 95 to 154 Sv [*Whitworth*, 1983; *Whitworth and Peterson*, 1985]. Referred to the deepest common level, the ACC average year-long total transport from six hydrography sections (1993-2000) along the WOCE line SR1b is 134 Sv, with a standard deviation of 11.2 Sv [*Cunningham et al.*, 2003]. The ACC transport is mainly carried in the SAF (53±10 Sv) and the PF (57.5±5.7 Sv). The baroclinic transport of the ACC above 3000 m has been steady between 1975 and 2000 and is 107.3±10.4. The frontal jets contribute 75% of the total baroclinic transport of the ACC but only occupy 19% width in Drake Passage [*Nowlin and Clifford*, 1982].

The FRAM simulations gave the total the ACC transport as 186 Sv, which is 50 Sv higher than the observations, while the baroclinic transport relative to 3000 db is 103 Sv compared with the observations of 107 Sv [*Grose et al.*, 1995]. This large

discrepancy in transport of the ACC in Drake Passage is believed due to the smoothness of the model topography, which results in some important topography features lost in simulation. However, POP results gave the ACC transport as 136 Sv from a ten year average despite higher zonally averaged wind stress [*Maltrud et al.*, 1998; *Best et al.*, 1999]. The better representation of the ACC transport in POP is believed due to the finer horizontal resolution and the unsmoothed bottom topography [*Best et al.*, 1999].

I.1.3 Transport and frontal variability in Drake Passage

The ACC transport time series from ISOS results are dominated in the subseasonal time scales (less than 2 months) by the lunar fortnightly and monthly tides and by baroclinic activity [*Peterson*, 1988]. Since the tides are in phase across the passage, the across-passage pressure variation from tides is small. The transport variability for seasonal time scales appears to be mainly barotropic, thus being well represented by bottom pressure records from each side of Drake Passage. The analysis also showed the seasonal sea surface variations across the current were driven by changes in wind stress curl associated with the subtropical highs and subpolar lows.

Hughes et al. [1999] proposed that the ACC transport fluctuations through Drake Passage, with periods between 10 and 220 days, are dominated by a barotropic mode that follows the planetary vorticity contours and suggested bottom pressure to the south of the ACC could be a good monitor of the ACC transport. *Hughes et al.* [2003] further pointed out the barotropic mode in subsurface sea pressure and the modeled the ACC transport fluctuations are closely related to the atmospheric forcing as represented by the Southern Hemisphere Annular Mode.

Despite the conclusion of steady baroclinic transport, *Cunningham et al.* [2003] argued that baroclinic variability is an important contribution to the ACC transport variability and that across-passage pressure difference is not an accurate indicator of variability in the ACC transport.

Nowlin and Clifford [1982] analyzed the hydrographical data and evaluated the mean width of each front. The average width of each front as measured across the Drake Passage is 51 km for the SAF, 61 km for the PF and 39 km for the SACCF

(called the Continental Water Boundary at that time). Strong velocity shear in the ACC leads to flow instability around the jets. *Inoue* [1985] calculated the first baroclinic Rossby radius of deformation varying from 17.3 km in the Subantarctic Zone to 7.5 km in the continental shelf. The small Rossby radius of deformation and strong vertical and horizontal shear in the Drake Passage might cause the frontal jets to develop baroclinic and barotropic instabilities.

Hofmann and Whitworth [1985] described the year-long current measurements at 500 meter in Drake Passage. The variations of SAF and the PF were mainly caused by meanders. The frontal meanders further developed into warm or cold rings. The existence of these rings in the PF Zone could cause the SAF to shift northward and the PF to shift southward. Several years of temperature anomaly time series at 2700 m reveal a 2-3 months period of warmer temperature anomaly, which may be related to the rings in the PF Zone. EOF analysis of the mooring currents reveals that the PF shifts with a time scale of about three months and that the shifting can penetrate to depths of 2500 m with 1 to 3 day time lag [*Klinck*, 1985; *Klinck and Hofmann*, 1986]. The mesoscale eddy time scales are mainly 1.5 to 2 months.

Observations and analysis have shown that the frontal variability was related to the topography at certain time scales. Modal decomposition showed that higher order baroclinic modes may be related to the steep topography [*Inoue*, 1985]. *Peterson et al.* [1982] described one cyclonic ring migration, subject to the modulation of the submarine ridge and topography gap aligned in the middle of Drake Passage. The moored current meter data from ISOS also showed that the alignment of seamounts might trap the rings passing by and retard the ring migration. EOF results revealed that the flow variations detected in the mooring array were triggered by the local bottom topography lee waves [*Klinck and Hofmann*, 1986].

WOCE line SR1b hydrography shows the PF location has a bimodal structure [*Cunningham et al.*, 2003]. However, this interannual variation of the PF seems not related to topography control, but related to the integrated baroclinic transport, temperature anomaly of AABW and AABW flux.

Sprintall [2003] analyzed six years of XBT measurements in Drake Passage to study the hydrographic variations in Drake Passage. The XBTs show no seasonal signals below 200 meters and there is little seasonal cycle evident in the location of

the fronts. The ACC baroclinic transport is deduced from the temperature and shows substantial variability on interannual time scales. No seasonal signal in the baroclinic transport is discernible.

Frontal locations in FRAM are not consistent with the observations [*Grose et al.*, 1995]. The PF exists in Drake Passage in the model as three jets. The total transport contained in the PF is only 40 Sv, small compared with the total transport of 186 Sv. Part of the PF transport joins with the SAF, and part of it joins with the SACCF. This discrepancy is mainly due to the smoothing topography in FRAM. The seamounts are smoothed in FRAM as one ridge and the PF is forced around the ridge and merges with the other two fronts. The variability of the ACC is still seen in this eddy resolving models; rings shed from the PF can propagate along the ridge northward. In the region that generates rings, the transport variability is also large. So the topography control for the frontal variability is also clear in the model result. The jet structure in POP is similar to that in FRAM, but generally with shorter length scale [*Sinha and Richards*, 1999].

I.2 RESEARCH OVERVIEW

I.2.1 General issues

There has been much debate and study on the frontal variability in the ACC. For different time scales, the variability seems to have different dynamics. One purpose of this research is to understand the forces causing frontal variations. Observations of the ACC variability in Drake Passage are ongoing today. But the observations are not sufficient to resolve these issues. Therefore, a fine grid modeling study of the ACC is a better alternative to help gain a synoptic view of the ACC fronts. One difficulty with modeling is establishing the validity of the results. This question is related to the required realism of the topography, forcing, boundary conditions and mixing schemes. At the very least, properly resolved bathymetry is required.

I.2.2 Research questions

1. How does the changing the ACC transport affect frontal variability ?

Are the ACC frontal locations affected by transport changes? How does eddy formation change with total transport? How does frontal meandering change with total transport?

2. How does the topography affect the frontal variations?

   What are the roles of the seamounts, the ridges and the gaps in the frontal shifting and meandering, ring generation and propagation? How much form drag does the rugged topography in Drake Passage provide?

3. How does the wind stress affect frontal variations in Drake Passage?

   On what temporal scale does the wind stress affect the frontal variability? Can the surface stress balance the local form drag?

CHAPTER II

MODEL CONFIGURATION AND DATA ANALYSIS METHODS

II.1 MODEL DESCRIPTION

A regional ocean model and historical data (such as the World Ocean Atlas, ISOS, WOCE repeat lines, Southern Ocean Globec) will be used to investigate the research questions. The modeling could provide us abundant information on the ACC fronts and the frontal variations in different spatial and temporal scales. The historical data set can guarantee us the necessary initial conditions for the model and applied forcing (such as wind stress), and also provide us the real scenarios to test our model results. All the available information (simulation results and the available historical hydrographic data) will be analyzed to look at the frontal variability, the topography effects, the wind stress effects and the relationship among them.

The Regional Ocean Modeling System (ROMS) is a free-surface, hydrostatic, primitive equation ocean model that uses stretched, terrain-following coordinates in the vertical and orthogonal curvilinear coordinates in the horizontal. It was developed at UCLA and Rutgers University based on the S-coordinate Rutgers University Model. It has been completely rewritten and can be run efficiently in single or multi-thread computer architectures (*http://marine.rutgers.edu/po/index.php?page=RomsInfo&model=roms*). ROMS provides the user a variety of the numerical schemes, such as mixing schemes, pressure gradient schemes, advection schemes, etc., to match a specific problem.

ROMS uses the primitive equations of motion of sea water:

$$\frac{\partial u}{\partial t} + \vec{v} \cdot \nabla u - fv = -\frac{\partial \phi}{\partial x} + F_u + D_u \quad (1)$$

$$\frac{\partial v}{\partial t} + \vec{v} \cdot \nabla v + fu = -\frac{\partial \phi}{\partial y} + F_v + D_v \quad (2)$$

$$\frac{\partial T}{\partial t} + \vec{v} \cdot \nabla T = F_T + D_T \quad (3)$$

$$\frac{\partial S}{\partial t} + \vec{v} \cdot \nabla S = F_S + D_S \quad (4)$$

TABLE 1: The variables used in the numerical model.

Variable	Description
x, y, z	horizontal and vertical coordinates
t	time
u, v, w	the (x, y, z) components of velovity $\vec{v}$
$T(x, y, z, t)$	potential temperature
$S(x, y, z, t)$	salinity
ρ	in situ density
$\phi(x, y, t)$	dynamic pressure
D_u, D_v, D_t, D_s	viscosity and diffusion
F_u, F_v, F_t, F_s	forcing terms
f	Coriolis parameter

$$\rho = \rho(T, S, P) \tag{5}$$

$$\frac{\partial \phi}{\partial z} = \frac{-\rho g}{\rho_0} \tag{6}$$

$$\frac{\partial u}{\partial x} + \frac{\partial v}{\partial y} + \frac{\partial w}{\partial z} = 0. \tag{7}$$

where the variables are defined in Table 1, with the vertical boundary conditions: on the Surface: $(z = \zeta(x, y, t))$

$$\nu \frac{\partial u}{\partial z} = {\tau_s}^x(x, y, t) \tag{8}$$

$$\nu \frac{\partial v}{\partial z} = {\tau_s}^y(x, y, t) \tag{9}$$

$$\kappa_T \frac{\partial T}{\partial z} = \frac{Q_T}{\rho_0 C_P} + \frac{1}{\rho_0 C_P}(T - T_{ref}) \tag{10}$$

$$\kappa_S \frac{\partial S}{\partial z} = \frac{(E - P)S}{\rho_0} \tag{11}$$

$$w = \frac{\partial \zeta}{\partial t} \tag{12}$$

at the bottom: $(z = -h(x, y))$

$$\nu \frac{\partial u}{\partial z} = {\tau_b}^x(x, y, t) \tag{13}$$

$$\nu \frac{\partial v}{\partial z} = {\tau_b}^y(x, y, t) \tag{14}$$

$$\kappa_T \frac{\partial T}{\partial z} = 0 \tag{15}$$

TABLE 2: The variables used in vertical boundary description.

Variable	Description
$\tau_s{}^x(x,y,t), \tau_s{}^y(x,y,t)$	surface wind stress
ν	vertical viscosity coefficient
κ_T, κ_S	vertical diffusivity coefficients
ζ	surface elevation
h	water depth
$E-P$	evaporation minus precipitation
Q_T	surface heat flux
C_P	specific heat capacity of sea water
T_{ref}	surface reference temperature

$$\kappa_S \frac{\partial S}{\partial z} = 0 \tag{16}$$

$$-w + \vec{v} \cdot \nabla h = 0 \tag{17}$$

where the variables are defined in Table 2. ROMS uses a stretched vertical coordinate system, with the following transformation format:

$$\hat{x} = x \quad \hat{y} = y \quad \hat{t} = t \tag{18}$$

$$z = \zeta(1+s) + h_c s + (h - h_c)C(s) \quad -1 \le s \le 0 \tag{19}$$

$$\text{where C(s)} = (1-b)\frac{\sinh(\theta_s)}{\sinh(\theta)} + b\frac{\tanh[\theta(s+\frac{1}{2})] - \tanh[\frac{1}{2}\theta]}{2\tanh(\frac{1}{2}\theta)} \tag{20}$$

θ and b are surface and bottom control parameters, h_c is minimum water depth.

By using this transformation, the surface becomes $s = 0$ and the bottom becomes $s = -1$, which simplifies the vertical description and discretization. This simplification complicates the format of the primitive equations and boundary conditions. It also creates an error in the pressure gradient with high stratification and large topography slope.

ROMS uses a horizontal curvilinear coordinate system, which introduces two scale factors into the equations, that relate the differential distances to the actual arc lengths. This curvilinear coordinates allow ROMS to match any region on the Earth's surface which can be conformally mapped to a rectangular region.

After transforming to the vertically stretched and horizontal curvilinear coordinate

system, the primitive equations are discretized using a centered, second-order finite-difference scheme in the horizontal direction (Arakawa C grid) and the same staggered, second order finite-difference scheme in the vertical direction. Because free surface and baroclinic waves propagate at different phase speeds, the fast waves and slow waves in the model are split with the time step for each scheme controlled by the Courant-Friedich-Levy (CFL) stability condition. A third or higher order upstream bias scheme is used to achieve a better calculation of the advection terms.

In ROMS, the nonlinear equation of state for sea water is used to calculate density. ROMS uses potential temperature instead of in situ temperature, so it is necessary to convert the observed in situ temperature to potential temperature for the model.

ROMS reads input and writes output in NetCDF, a binary, self descriptive data format. It uses almost half of the disk space compared to the ASCII format and one can retrieve the attribute information from the data file with the self descriptive properties of the format. The initial forcing and assimilative (or nudging) data used in ROMS must be prepared in netCDF format as model input. The output data from ROMS are also provided in netCDF format.

II.2 MODEL CONFIGURATION

II.2.1 The study area, model domain and bathymetry

The model domain must cover the main bathymetric features in Drake Passage (Fig. 2). Most global ocean models use the Mercator projection to generate horizontal grids or spherical coordinate for model grids. The consequence is that adjacent grid spacing differs which causes additional consideration and numerical errors. The grid in this study uses a stereographic projection centered on 58°S, 62°W with an anticlockwise rotation of 30° and an almost uniform grid spacing. The rotation of the model domain allows the ACC to enter the domain approximately normal to the western model boundary. Another advantage of such a projection is that the horizontal grid spacing is nearly homogeneous in both directions.

This modeling study will use a 6 km grid resolution to reduce the computational time and still keep the basic topographic features. Our study focuses on frontal jets

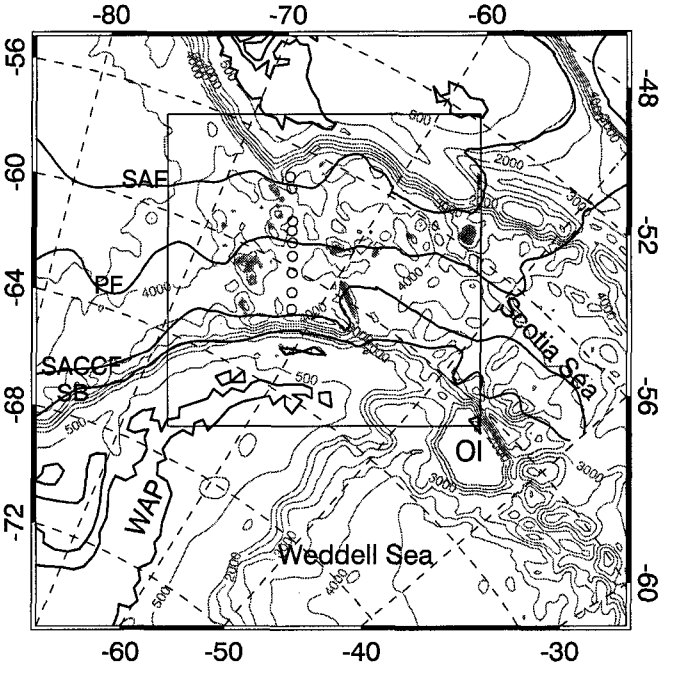

FIG. 2: The model domain is the 1200 km by 1200 km box in the middle of the map. The historical frontal locations are indicated as heavy lines. Shading shows bathymetry shallower than 3500 m indicating the seamounts in the middle of Drake Passage and Shackelton Fracture Zone. The open circles are the ISOS mooring array locations. OI is the Orkney Island and WAP is the Western Antarctic Peninsula.

and eddies generated from them, both of which usually have spatial scales larger than 30 km [*Peterson et al.*, 1982; *Gille*, 1994]. The grid spacing of 6 km is appropriate so that more than 5 grid points could span the frontal jets or eddies.

The 2 minute resolution bathymetry data set ETOPO2 (2 minute gridded Earth Topography) [*Smith and Sandwell*, 1997] from the National Geophysical Data Center is used for the model bathymetry. These data were derived from satellite gravity observations combined with quality-assured shipboard echo-sounding measurements. The 2 minute data are mapped to the model grid by linear interpolation. The main features of the Drake Passage topography, such as the seamounts, ridges, and gaps can be better constructed in the model (Fig.2).

The S coordinate model requires smooth bathymetry to reduce the pressure gradient errors. To assure a stable model simulation, the maximum slope parameter $|\Delta h/2h|$ should not exceed 0.22 and the hydrostatic consistency parameter $|\sigma\Delta h/h\Delta\sigma|$ should not exceed 1 [*Haidvogel and Beckmann*, 1999; *Mellor et al.*, 1998]. To achieve such criteria, the Shapriro-based filter is applied to the model topography [*Hedstrom*, 2000]. This filtering reduces the height of the seamounts and ridges and the depth of trenches.

II.2.2 The initialization and the feature model construction

For large scale circulation, an objectively analyzed climatology, such as World Ocean Atlas (WOA) [*Boyer and Levitus*, 1998] is usually used for model initialization and boundary conditions. This data set is based on the historical measurements and averaged both spatially and temporally. In Drake Passage, due to frontal shifting and meandering, this averaging of observations smooths the frontal features. This initialization for a regional model is not appropriate. Therefore, a feature model of fronts is used to create a more realistic initial state to study the ACC frontal variability in Drake Passage. Without data assimilation, a physically meaningful initialization can improve the predictive capacity in a regional ocean model [*Gangopadhyay et al.*, 1997].

This kind of initialization can also be achieved by setting up a feature model. The feature model is based on observations in a specific region, initialized with the

main features of local hydrographic data and dynamically adjusted for the mismatch between the hydrography and circulation. The feature model can provide the multi-scale current or water mass features so simulation of interaction among these features with different temporal and spatial scales is time-saving and convenient. The feature model has been used in mesoscale eddy prediction, frontal dynamics and ecological coupling with frontal jet [*Gangopadhyay et al.*, 1997, 2002; *Lima et al.*, 2002].

II.2.3 Surface, bottom forcing and mixing scheme

For only looking at the frontal variability in Drake Passage under the effect of the variable transport, we did not specify any surface forcing. This does not mean that the circulation is not wind driven since the volume transport imposed along the western boundary is due to wind stress over the Southern Ocean. For the bottom stress, the linear form of bottom friction is used in these experiments.

For some cases, the wind stress is applied at the surface to look at the frontal variations due to local wind stress effects. The 6 hourly and smoothed wind stress are bilinearly interpolated into the model grids using the forcing pre-processing package provided with ROMS. The wind stress data are blended wind data from QuikSCAT (QSCAT) dataset and National Centers for Environmental Prediction (NCEP) re-analysis dataset [*Milliff et al.*, 2004].

The K-Profile Parameterization (KPP) vertical mixing scheme is used throughout. We do not specify the surface flux of heat or fresh water. The horizontal viscosity coefficient is set proportional to the diagonal grid spacing with a maximum value of 50 $m^2 s^{-1}$ and the diffusivity coefficient is set to a tenth of viscosity.

II.2.4 Boundary conditions and the open boundary problems

Open boundary always causes problems for numerical models. For a regional ocean model, we adopt the relaxed boundary conditions similar to that used by *Marchesiello et al.* [2001]. The temperature and the salinity are relaxed to climatological values along each open boundary with a short nudging time scale of 5 days. Nudging extends into the interior for 10 grid (~60 km) to prevent the eddies approaching the boundary. A constant 2D vertically integrated velocity described in the next chapter is relaxed

into the model domain using the same nudging time scale. The free surface boundary has zero gradient boundary conditions, which cause a drift of free surface over a long model run. Total volume conservation is imposed in the model to prevent the surface drift. With these boundary conditions the model can run stably.

Land boundary conditions are set to no-slip, which means that the three components of velocity are zero on the land boundaries.

II.3 AN OVERVIEW OF THE MODEL SIMULATIONS

The model simulations are categorized into two groups to look at the following factors affecting the frontal variability: the transport, the wind stress and the bathymetry.

The ACC fronts in Drake Passage often failed to appear realistic in global ocean circulation models [*Thorpe et al.*, 2005]. The SAF behaves better due to the confinement of the northern wall (the South America continent) in Drake Passage. The PF tends to shift farther south or join the SAF. The transport distributed to each ACC fronts in models do not always have the same values as observations [*Grose et al.*, 1995].

II.3.1 The effect of transport variation

The estimated total ACC transport from ISOS ranges from 95 Sv to 154 Sv [*Whitworth and Peterson*, 1985], while from Lowered Acoustic Doppler Current Profiler (LADCP) measurements the total transport ranges from 95 to 184 Sv [*Cunningham et al.*, 2003]. The larger range for LADCP may be due to larger errors. The ACC transport in Drake Passage varies over a large range of 50 to 60 Sv. To look at the effect of total transport variation on the frontal locations, we specify the total transport from 95 Sv to 155 Sv with an interval of 10 Sv, and let the model run for about 400 days to look at the frontal variations. Though longer time can be achieved for large transport cases, the open boundary conditions do not behave perfectly with small transport (especially for 95 Sv,105 Sv) and the model may blow up soon after 400 days due to unrealistic propagation of the baroclinic processes cross the boundary. For each case, the temperature and salinity will have the same initial values to match a relatively

steady baroclinic transport. In total, we have 7 simulations for this purpose. The same bathymetry is used for each simulation so that only the transport effects are examined.

II.3.2 Influence of wind stress

QSCAT/NCEP blended wind stress data is applied in the model to look at the wind stress effects on the frontal variations. Since we only look at the frontal locations due to the effects of different wind stress, we run the model for the transport case of 135 Sv. Three different cases are considered: Original wind stress, monthly running mean filtered wind stress and no wind stress situations. These simulations use different initial and boundary data. Details of the setup will be given in Chapter 4. Each simulation runs for 5 years and the wind stress is only applied during the fifth year.

II.4 VALIDATION OF MODEL RESULTS

In addition to the accuracy of the numerical model solving the realistic problems, we have other issues in the construction of a reasonable initial and boundary conditions (both horizontal and vertical). Validation of the model results by comparing to observations is necessary.

The sea surface height anomaly from satellite measurements can be used to validate the model sea surface height anomaly. The large scale anomalies, such as the propagation of the Antarctic Circumpolar Wave, do not appear in our model. The comparison should focus on the regional anomalies which are related to the topography modulations and the frontal dynamical adjustments.

Hydrographic transects across Drake Passage can be retrieved from the WOA98 dataset. The transects run from late 1970s until the present day, though very sparse in time. These data are used to compare the vertical structure of the model hydrography.

II.5 DIAGNOSTICS OF THE MODEL

II.5.1 Kinetic energy

The model reaches a dynamically steady state when the volume averaged kinetic energy approaches a steady value. The conversion between available potential energy and kinetic energy should be reflected in the kinetic energy curve. We will analyze each kinetic energy curve to look at the circulation variations.

The conversion between kinetic energy and available potential energy is examined over each front. Development of kinetic energy over each front is used to indicate the state of the front.

II.5.2 Ertel potential vorticity

Ertel potential vorticity (EPV) is an important physical variable in oceanography and atmospheric science. EPV is defined as $q = \frac{(\vec{f}+\vec{\zeta})\cdot\nabla\theta}{\rho}$, where q is EPV, $\vec{f}$ is the planetary vorticity, $\vec{\zeta}$ is the relative vorticity, θ is the conserved quantity, here chosen as the potential density, and ρ is the density. Under adiabatic conditions and no external forcing, the EPV is conserved along the track of a water parcel [*Gill*, 1982]. Usually, in deep water, these conditions are met and EPV is regarded as conserved. EPV can be used to track water masses and distinguish different water bodies, such as the distinct difference of waters on each flank of one front. Due to its conservative properties, EPV should be correlated to the stream function. A relationship between them is examined with least square statistical methods.

II.6 ANALYSIS OF MODEL RESULTS

Surface height streamlines are used to locate the fronts since the large lateral surface elevation gradient usually corresponds to a narrow range of the sea surface height streamlines [*Sokolov and Rintoul*, 2002]. Highest temperature gradient and temperature isotherm are also used to locate the fronts at 500 m. The frontal location shift is examined with the total transport specified on the western boundary. This includes

the mean position and the deviation of the three frontal locations relative to their historical locations.

The influence of topography on frontal variability is investigated. Since Drake Passage bathymetry is very complicated, the flow close to steep topography is examined carefully. Planetary vorticity will be used to analyze flow variations.

We calculate the surface stress and the bottom skin and form drag. The form drag can be expressed as a function of bottom pressure and topography [*Edwards et al.*, 2004] as $\int_{A_0} \frac{P'_B}{\rho_0} \nabla h dA$, where A_0 is the horizontal projection of topography, P'_B is bottom pressure anomaly, ρ_0 is mean density, and h is bottom topography. We will examine the form drag in Drake Passage and compare it with the local wind stress to understand the role of the topography in Drake Passage on ACC dynamics.

We look at the correlation between the local wind stress and the PF locations to investigate how the local wind stress affects the local dynamics.

Since there exists a discrepancy between the surface expression and the subsurface expression for the PF, we compare the frontal locations at the surface and at 500 m for various conditions. Usually, the surface front locations are obtained from surface elevation, while the 500 m front locations are obtained from the temperature fields. Whether the wind stress has an effect on the discrepancy in the surface and subsurface expression of fronts are examined.

CHAPTER III

TRANSPORT EFFECT ON FRONTAL VARIABILITY

In this study, we use a high resolution, regional ocean circulation model to study the relationship between the volume transport of the ACC and front variability. By specifying different transport along the western boundary, we look at how each ACC front in Drake Passage responds.

The first section describes the model that we use along with details of initial and boundary conditions. The following section presents the diagnostics that we use to analyze the model. Section 3 presents results from the various simulations that we run. Section 4 discusses the implications of these results, followed by section 5 which recaps the main conclusions.

III.1 MODEL DESCRIPTION

Initial distributions of temperature and salinity are taken from the World Ocean Atlas [*Boyer and Levitus*, 1998]. However, time and space averages of sparse observations in this region with frontal variability produce weak property gradients instead of sharp, narrow frontal features. We use a feature model (similar to that of *Gangopadhyay et al.* [2002]) to recover the fronts at their mean locations. We assume that properties in the fronts follow an error function consistent with a Gaussian frontal jet as described in *Gille* [1994].

The feature model is constructed as follows. The temperature and salinity from the World Ocean Atlas within each frontal zone is averaged along the front. The error function is used to construct the fronts as: $T(\vec{r},z) = T_1(z) + (T_2(z) - T_1(z))\psi((\vec{r}-\vec{r_0})/\sigma)$, where $T(\vec{r},z)$ is the temperature or salinity at location $\vec{r}$ and depth z, $T_i(z)$ represents the temperature or salinity on each side of the front, ψ is the error function and $\vec{r_0}$ is the location of frontal axis. The frontal width is chosen to be 51 km for the SAF, 61 km for the PF, 39 km for the SACCF, 30 km for the Southern Boundary to be consistent with hydrographical measurements by *Nowlin and Clifford* [1982].

Along the open boundaries, the temperature and salinity are relaxed to the initial conditions for these variables. The nudging time scale is 5 days. Nudging is imposed over a zone of about 30 km thickness over most of the model grid next to the open boundary. A 60 km (10 grid intervals) zone is imposed at the eastern boundary to improve model stability. The free surface condition at the boundaries is no-gradient. The total volume transport at the model boundary is controlled to keep a balanced inflow and outflow.

The geostrophic velocity is calculated along each boundary from the initial temperature and salinity referenced to 2500 m. Vertically integrating the geostrophic velocity, we obtain the 2D integrated baroclinic flow along the boundary and the baroclinic transport. We add barotropic flow with the same shape as the baroclinic flow to match the desired total transport. The combination of the baroclinic and the barotropic flow is imposed along the boundary. The imposed incoming volume transport represents the effect of the Southern Hemisphere winds on the transport through Drake Passage.

No wind stress is applied within the model domain. Experiments adding local wind forcing have solutions very similar to those presented here. Bottom stress is applied as the linear function of the bottom velocity with a drag coefficient of 0.0025. The horizontal viscosity is 50 $m^2\ s^{-1}$, and the tracer diffusion coefficient is 5 $m^2\ s^{-1}$. A K-Profile Parameterization (KPP) vertical mixing scheme is used.

Seven Model simulations are run for different imposed transport which range from 95 Sv to 155 Sv with an interval of 10 Sv. In each transport case, the model begins in a static state with the same featured initial conditions and runs for 400 days. The model state is saved every 5 days.

III.2 MODEL DIAGNOSTICS

III.2.1 Kinetic energy and potential energy

The volume averaged total energy is an important indicator of the model state. These simulations are driven largely by kinetic energy input through the western boundary and kinetic energy dissipation due to bottom and interior frictional losses. Energy

converts between kinetic and potential due to a variety of mixing, geostrophic adjustment and dynamic instability mechanisms. The energetics are analyzed by calculating the volume averaged kinetic energy (VAKE) and volume averaged potential energy (VAPE) at each time the model state is saved. The specific calculations are

$$VAKE = \frac{0.5 \cdot \sum\sum\sum \rho_{i,j,k}(u^2_{i,j,k} + u^2_{i+1,j,k} + v^2_{i,j,k} + v^2_{i,j+1,k})\Delta z \Delta x \Delta y}{\sum\sum\sum \Delta x \Delta y \Delta z} \tag{21}$$

$$VAPE = \frac{\sum\sum\sum \rho_{i,j,k} g z_{ri,j,k} \Delta z \Delta x \Delta y}{\sum\sum\sum \Delta x \Delta y \Delta z} \tag{22}$$

III.2.2 Frontal kinetic energy

The volume averaged energetic quantities provide general information on the model state, but the transport and kinetic energy are mainly found in the fronts so it is necessary to delineate each frontal area and calculate quantities within the frontal areas.

We define each front by two sea surface elevations. Since we use the strong nudging/clamped boundary conditions on the western boundary, the surface elevation and temperature on the surface are maintained through the domain with the step-like structure imposed at the boundary. The peaks in the surface elevation gradient along the western boundary are consistent with the location of the fronts. Centered at this point, we locate two grid points at the boundary whose distance is approximately equal to the frontal width. Contour lines corresponding to these surface elevation values denote the front. A flood-fill method is used to mark the area between these two bounding lines. The frontal surface area and VAKE in these areas are calculated for each frontal area.

The PF and SAF are easily demarked by this method. However, the SACCF is more difficult to delineate. In addition, it makes a smaller contribution to the transport and energy, so the calculation is not done for the SACCF.

III.2.3 Tracking fronts from surface elevation and temperature at 500 m

Over the Southern Ocean, the surface elevation and temperature may change along a frontal axis [*Dong et al.*, 2006]. However, over short distances the surface elevation

is a good indicator of a front. *Sokolov and Rintoul* [2002] found a narrow range of SSH values corresponds to the largest lateral SSH gradient. Fitting elevation to the error function is used to track the location of fronts [*Gille*, 1994]. The surface density (imposed at the western boundary) in the model solutions remains approximately fixed along streamlines. Surface elevation is a close proxy for the circulation, so the surface elevation isoline can be used to locate the front throughout the model domain.

Because of this relationship, the frontal axis can be tracked using the surface elevation value defined on the western boundary. Different transport cases have different surface elevation values for the fronts. Due to the no-gradient boundary condition, the defining surface elevation for a front changes slightly with time. To obtain the appropriate elevation for a frontal axis, we define the fronts for each model state (starting with the second simulation month) and calculate an average and variance for the frontal position along the y axis (typically using more than 70 values for each simulation). The frontal locations are assumed to be single valued functions of the model x coordinate, so strong meanders are not represented. If there is a meander in the front, the southern most point is taken as the frontal location as in *Dong et al.* [2006].

Since there is little seasonal temperature variation below 200 m [*Sprintall*, 2003], the temperature at 500 m is a good way to locate fronts over time. The 500 m temperature from the ISOS moorings was used to track the PF [*Hofmann and Whitworth*, 1985] over a 14 month period. Similarly, in the model 500 m temperature is used to track the PF using a target temperature associated with the front defined on the western boundary. The same temperature was used for a given front for different transport cases. As with surface elevation, the target isotherm was assumed to be a single valued function of the model x coordinate.

III.2.4 Calculation of the PF shifting distance

The PF shift distance is the difference of the simulated front location and the historical location [*Orsi et al.*, 1995], or $SD = \sum |\vec{r} - \vec{r}_0|/N$, where $\vec{r}$ is the PF location for each x grid index I, $\vec{r}_0$ is the historical PF location at the same index, and N is total x direction grid points (excluding nudging and sponge layers). The model solution in the first month is not used due to model adjustment. This diagnostic is used to

estimate the effect of imposed ACC transport on frontal location and variability.

III.3 MODEL RESULTS

Model simulations are run for one month to allow the initial fronts, specified by the feature model, to come to a geostrophic balance. Model results from the end of the first month to day 400 are analyzed. For each of the simulations with different imposed transport, we analyze the integrated energy, compare the frontal locations to climatology, compare surface elevation to satellite observations and analyze EPV.

III.3.1 Kinetic and potential energy analysis

VAKE behaves differently for different transport cases (Fig. 3a). For all cases, VAKE generally increases with time and oscillates but there is no tendency for VAKE to increase with increasing transport (although the case with the largest transport has a much larger excursions of VAKE than the other cases). The trend in the VAKE indicates the model does not reach a stationary state. In fact, VAKE increases over time as the frontal jets become unstable and develop mesoscale variability. The model may need longer time to adjust itself to the imposed boundary conditions. The variation in the VAKE (especially for the SAF) is from the baroclinic process in the interior of the model domain, and partially due to the open boundary conditions (see the discussion [*Marchesiello et al.*, 2001]).

The total input kinetic energy for these different transport cases must be balanced by some other mechanisms besides geophysical adjustment to frontal kinetic energy, such as increasing of dissipation rate due to increased vertical shear or an increase in bottom form drag.

VAPE decreases with time for all transport cases with the smaller transport cases declining more than the higher transport. The amount of VAPE reduced with time ranges from 100 kg m^2s^{-2} with 155 Sv transport to 600 kg m^2s^{-2} with 95 Sv. These numbers are much higher than the amount of increase in VAKE (order of 10 kg m^2s^{-2}). This reduction in VAPE is associated with reduced pycnocline slope, which is due mainly to active mixing process.

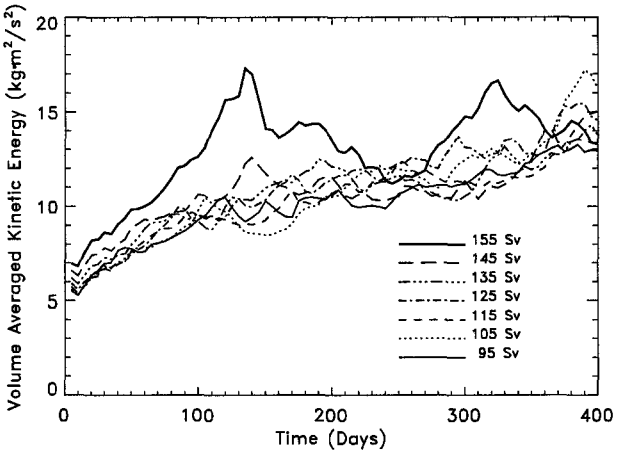

(a) Volume Averaged Kinetic Energy

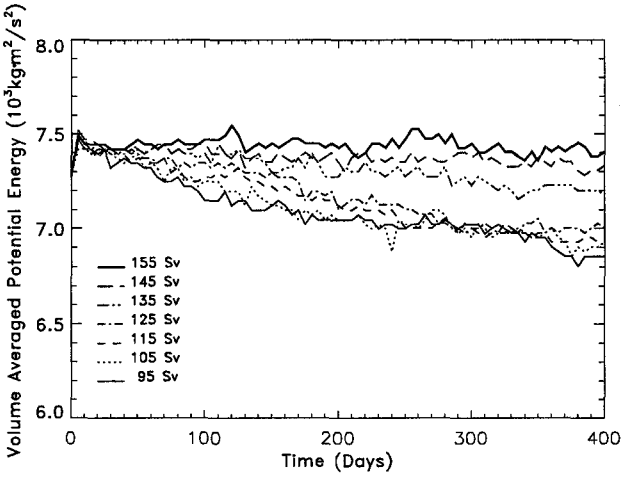

(b) Volume Averaged Potential Energy

FIG. 3: Volume averaged kinetic and potential energy over the whole model domain. The units of VAKE in the plot are 1000 kg m^2 s^{-2} and a constant number is subtracted to better see the variability.

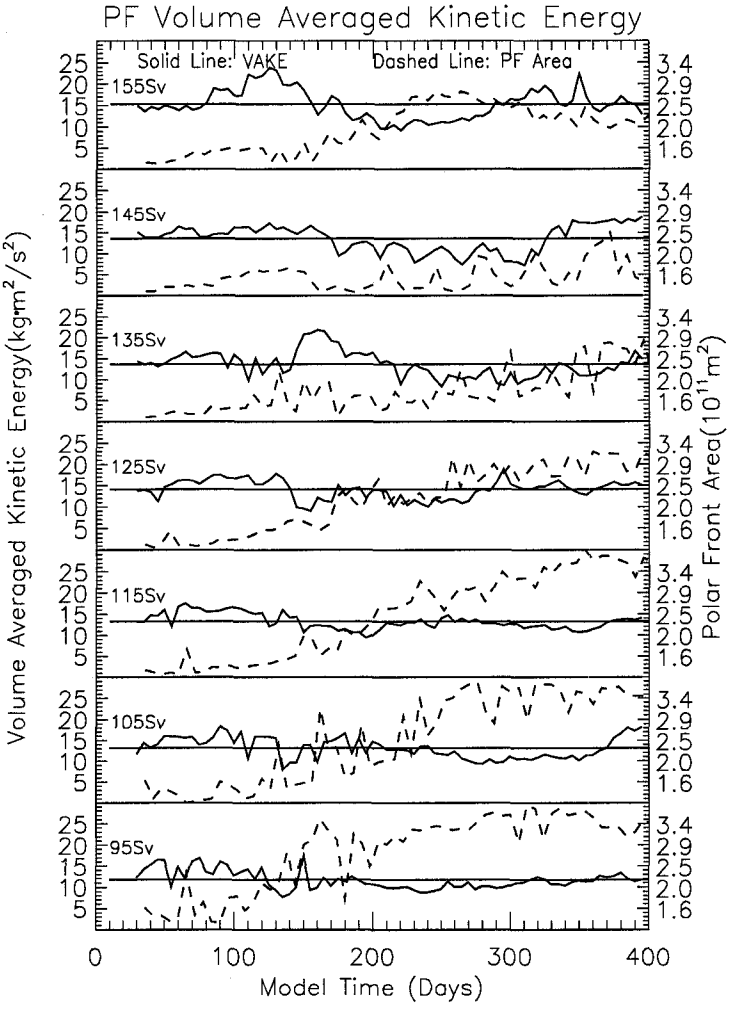

FIG. 4: The volume averaged kinetic energy and area of the Polar Front. The solid line is the volume averageD KINetic energy. The dashed line is the frontal area. The straight solid line is the time mean VAKE.

The VAKE in each front is relatively steady (Figs. 4 and 5) compared to the whole domain VAKE (Fig. 3). This steadiness indicates that the PF and SAF have adjusted to a geostrophic balance during the first month. Thus, the VAKE in zones between fronts must increase to account for this difference. This increase must be caused by transfer of kinetic energy from the fronts due to shedding of meso-scale eddies. This process mixes waters across the fronts and tends to diminish the isopycnal slope in the fronts.

The area of the PF increases over time for all transport cases. This increase is due

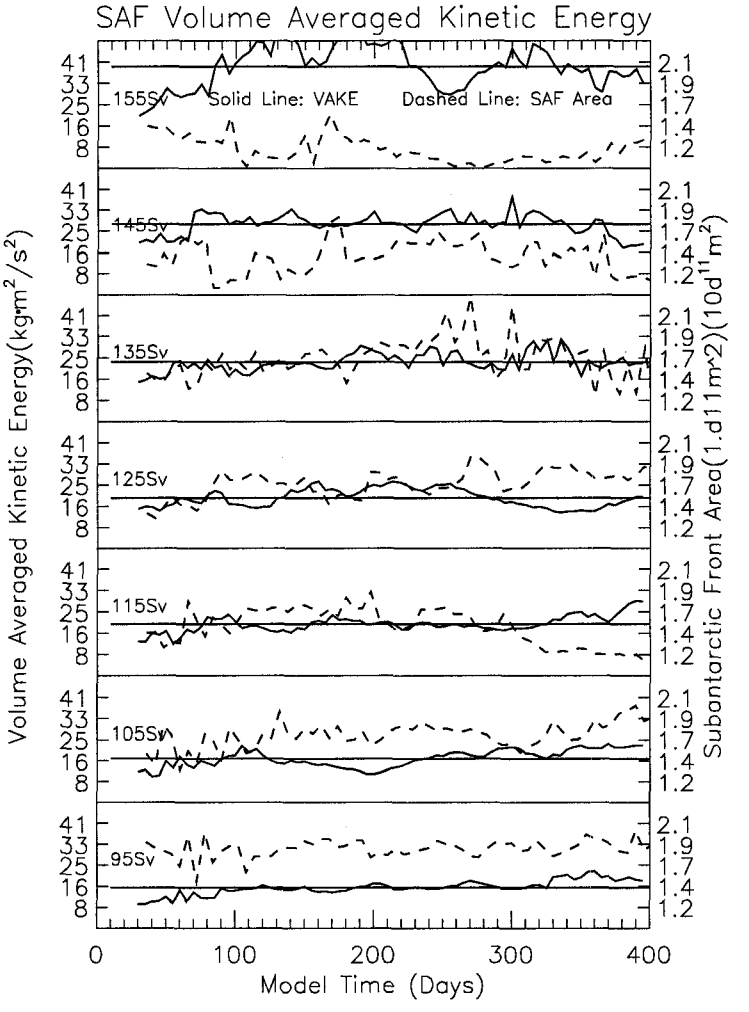

FIG. 5: The volume averaged kinetic energy and area for the Subantarctic Front. The solid line is the volume averaged kinetic energy. The dashed line is the frontal area. The straight solid line is the time mean VAKE.

to mesoscale eddies, which is clear from model snapshots except close to the nudging and sponge layer where it converges to the specified location on the eastern boundary. Longer running cases (up to 4 years) develop an increasingly wide PF due to eddy shedding to the point that the PF is difficult to detect (figures not shown). Over these long simulations, the PF in the model reappears as a frontal jet but remains weaker than the SAF.

The VAKE for the SAF increases with increasing transport implying that the velocity of the SAF jet increases. The area of the SAF stays relatively steady. The highest transport case (155 Sv) shows a reduction of the SAF area compared to other transport cases in spite of the higher VAKE, indicating that the eddy shedding must decrease.

Unlike the PF, the SAF can not shed its additional KE through shedding of rings due to the close proximity of the continental slope at the north side of Drake Passage. This tendency is indicated by the relatively constant frontal area for the SAF (Fig. 5).

III.3.2 Surface elevation comparison with satellite data

The observed surface elevation is obtained from AVISO Ssalto/Duacs which provides weekly global gridded ($1/3° \times 1/3°$) absolute surface dynamic topography. This field is constructed from data from all altimeter missions (Jason-1, Topex/Poseidon, Envisat, GFO, ERS-1 & 2 and even Geosat) and the mean dynamic topography data Rio5 (a combined product recovering 7 years (1993-1999) based on GRACE mission, altimetry and in situ data).

The AVISO data is extracted over the model domain and averaged for 5 years (Fig. 6a). Frontal locations are not clearly evident due to averaging, but some basic features remain. The separation of the SAF and the PF in the middle of Drake Passage can be seen. The remarkable northward excursion of the SACCF occurs after passing the Shackelton Fracture Zone (around 58°W,60°S). In the west, fronts are not distinguished clearly from the mean SSH fields due to the high spatial variability there.

The surface elevation from the model solutions are averaged for one year (Fig. 6b-h). We label each front in the mean fields with one surface elevation isoline which

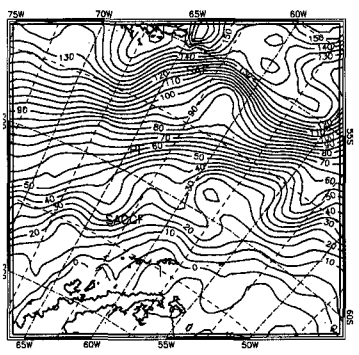

(a) AVISO Mean SSH

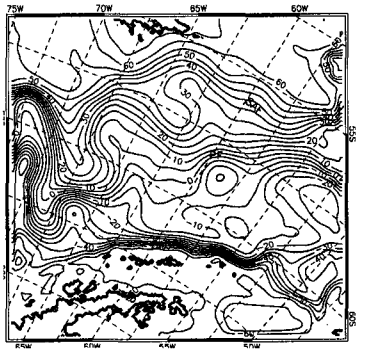

(b) Modeled Mean SSH 095 Sv

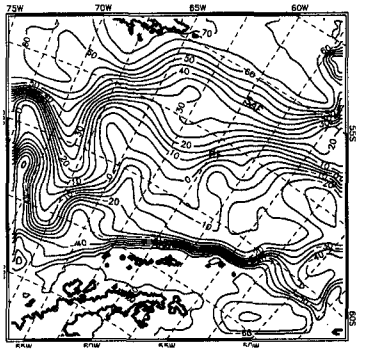

(c) Modeled Mean SSH 105 Sv

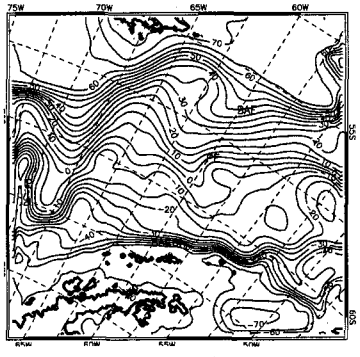

(d) Modeled Mean SSH 115 Sv

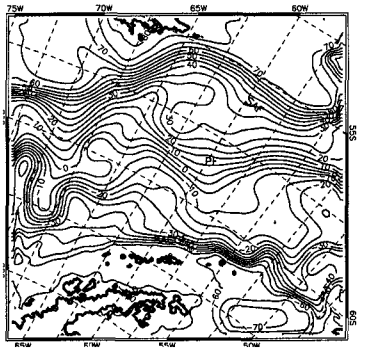

(e) Modeled Mean SSH 125 Sv

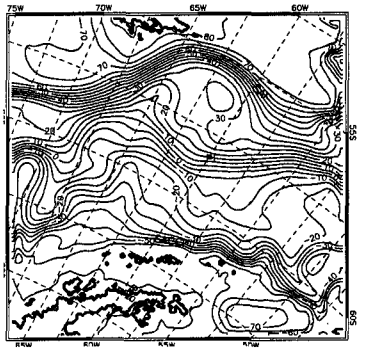

(f) Modeled Mean SSH 135 Sv

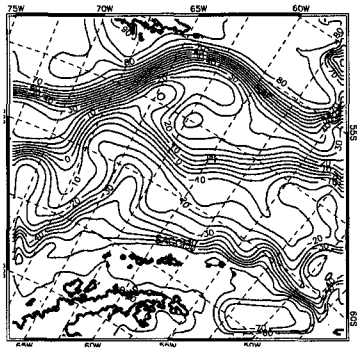

(g) Modeled Mean SSH 145 Sv

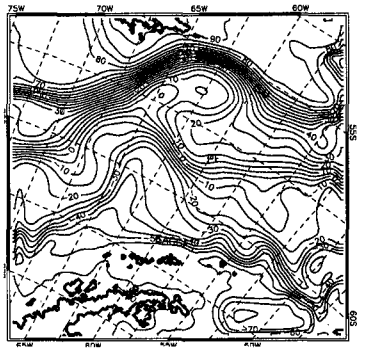

(h) Modeled Mean SSH 155 Sv

FIG. 6: Time mean sea surface height from observations (AVISO) and model results. Contours represent sea surface elevations in AVISO and the model, respectively. The weekly observed altimetry data is averaged over the time from 09/2001-07/2006. Model results were averaged from day 31 to day 400.

is the mean of the frontal axis surface elevations. Each front is easily located in the mean SSH fields. The strongest frontal jet is associated with the SAF.

The PF shows clear differences in cases with different transport. With the higher transport, the PF is narrower than with smaller transport.

The large meanders occur in the SAF and PF near the western boundary for the smaller transport cases (95 Sv to 125 Sv). The SACCF shifts more northward with higher transport.

A quantitative similarity comparison is made between modeled mean SSH image and AVISO image in Fig. 6. A method usually used to detect the structure similarity between two images [*Wang et al.*, 2004] is used here to detect the similarity (or difference) between the SSH fields. Details of the method can be obtained from *Wang et al.* [2004] and *http://www.cns.nyu.edu/~lcv/ssim/*. The structure similarity index (SSIM), usually between -1 and 1, is obtained to display the structure difference in the satellite image and the model results (Fig. 7). At the regions close to the SAF and the SACCF, SSIM is close to 1 and shows similar structure between the mean AVISO and the model results. The lower SSIM (usually less than 0) occurs at the PF region, which is associated with the PF variability with different transport and the much smoothed AVISO data. Close to the western boundary, the SSIM also shows small value, which affects the difference from the boundary effect. With higher transport cases, the PF looks more similar to the AVISO fields from SSIM index than with smaller transport.

To avoid the problem of time averaging, two instantaneous fields are compared, one from the satellite and one from the model (Fig. 8). These fields are more similar than the mean fields. The SAF is the strongest current jet in both fields. The strong meander of the SAF was not always present in the model but did occur at times with a pattern like that in the observations (figure not shown).

For larger transport, the fronts (PF and SAF) have smaller meanders and seem more stable upstream of Drake Passage. The SAF show meanders in Fig. 8b. The model frequently spawns warm eddies from the SAF at this location.

One notable feature in AVISO altimetry is the splitting and rejoining of fronts. In the satellite field, the PF enters Drake Passage and splits into several filaments

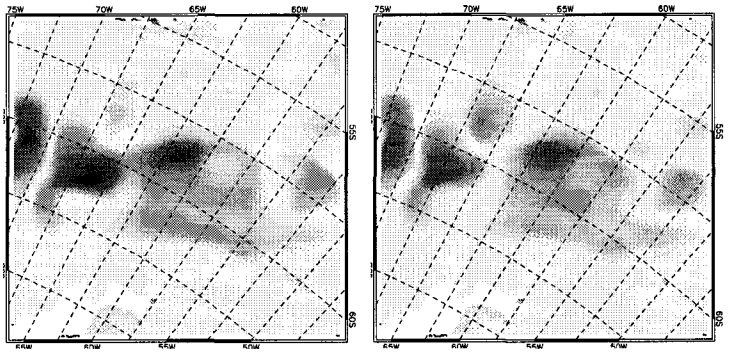

(a) Modeled Mean SSH 095 Sv

(b) Modeled Mean SSH 105 Sv

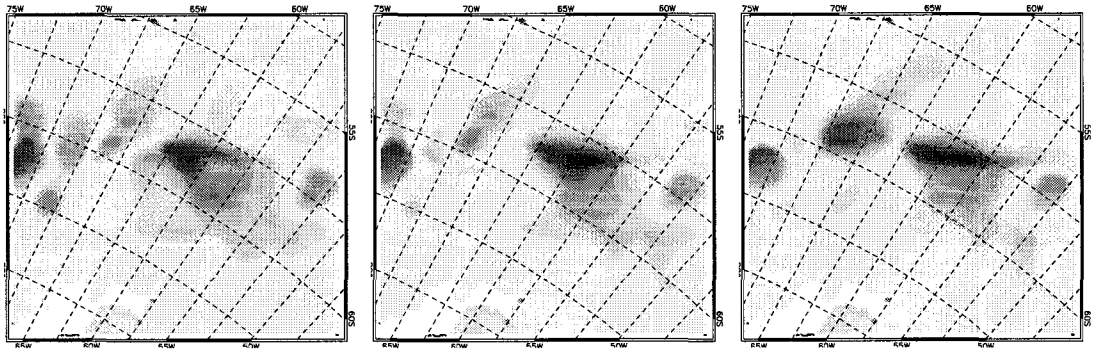

(c) Modeled Mean SSH 115 Sv

(d) Modeled Mean SSH 125 Sv

(e) Modeled Mean SSH 135 Sv

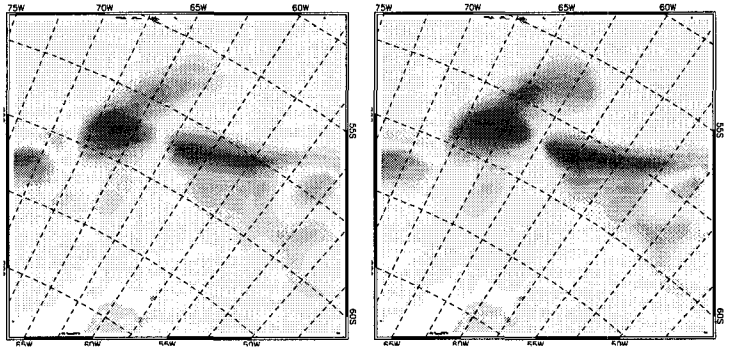

(f) Modeled Mean SSH 145 Sv

(g) Modeled Mean SSH 155 Sv

FIG. 7: SSH structure similarity index (SSIM) between the mean AVISO SSH and the modeled mean SSH with each transport case in Fig. 6. White color represents identical structure, where SSIM is 1. Black represents completely different structure, where SSIM is -1.

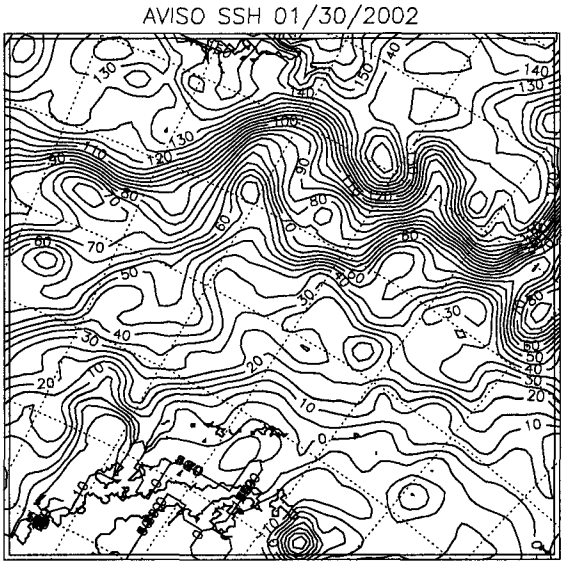

(a) AVISO SSH on 01/30/2002

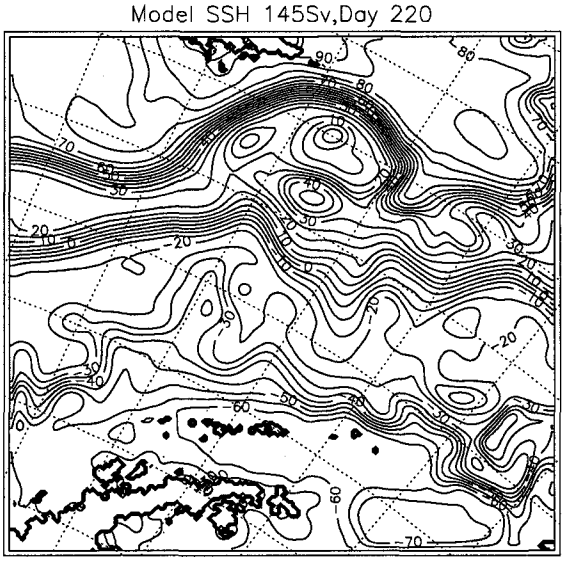

(b) Model SSH 145 Sv on Day 220

FIG. 8: Observed sea surface height for Jan 30, 2002. Model sea surface height for day 220 for the 145 Sv case.

when passing the seamounts ($65°W, 61°S$) in the passage. These filaments rejoin downstream. In the model, the PF occurs as a very strong jet upstream and does not split over the seamounts. Eddies are generated downstream of the seamounts.

The observed SACCF shifts northward due to the Shackelton Fracture Zone ($58°W, 59.7°S$) and returns to south after this area. The modeled SACCF loses this excursion which is also a feature of other GCM solutions [*Thorpe et al.*, 2005].

The weekly AVISO data we used have the resolution of $1/3° \times 1/3°$ and are gridded from different time and space and different altimeters. Aliasing due to low resolution gridding and weekly averaging exists in the data due to the high frontal variability.

III.3.3 Surface elevation tracked fronts

The mean frontal locations for the different transport cases are compared to their historical mean locations (Fig. 9a-c). The basic tendency is that the mean frontal axis stays northward with higher transport and southward with smaller transport in the middle region of the Drake Passage. The distance of the mean location from its historical location is not the same for the three fronts in the same transport cases. We see the largest moving distance occurs for the PF, which is the most unstable front in the model.

The largest shift of the PF occurs in the middle of Drake Passage where the topography is relatively flat. The mean location difference for 95 Sv and 155 Sv can be as large as 300 km. For the 145 Sv and 155 Sv transport cases, the mean PF locations are north of the historical location. For the 135 Sv transport case, the mean PF location is north of the historical location in the upstream part of the model while staying to the south a small distance on the downstream side. For other transport cases, the PF stays to the south of the historical location, though for the 125 Sv transport case the mean location is very close to the historical location upstream. It should be kept in mind that we average the frontal location along the longitudinal line (constant x), so the large fluctuations of the front (S shape) are not seen in these mean locations.

The SAF moves a small distance northward for transport larger than 135 Sv, while for smaller transport it stays to the south. It is likely that the northward shifting

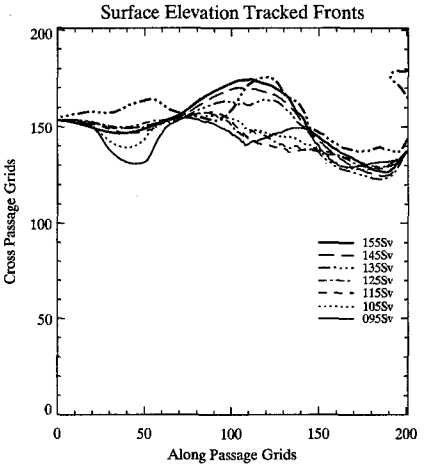

(a) Subantarctic Front

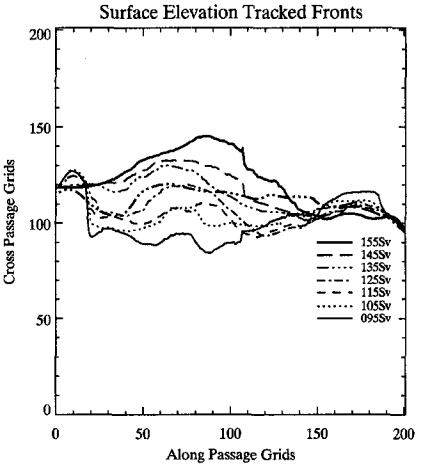

(b) Polar Front

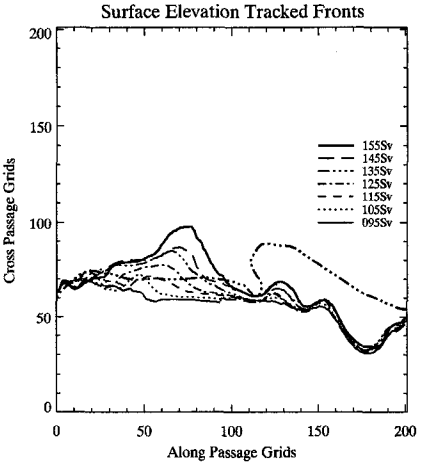

(c) Southern ACC Front

FIG. 9: Frontal location based on sea surface height. The thick dash-dotted lines are the historical locations of the fronts from *Orsi et al.* [1995].

with larger transport is blocked by the northern wall in the model. The upstream southward meander is also related to the transport. This meander is small with large transport, and big with small transport. This feature can also be seen in the mean SSH fields (Fig. 6b-h).

The SACCF, in the western region, moves northward after passing the seamount area. The northward movement is related to the spawning of the cold eddy from southern side. These cold rings move northward along the eastern flank of the seamount area, which is consistent with the eddies/rings movement from ISOS observations [*Hofmann and Whitworth*, 1985; *Peterson et al.*, 1982]. While on the eastern side of the model domain, the SACCF goes against the southern wall and has little meandering and does not appear consistent with the northward excursion observed in the historical hydrographic measurements. We did not observe in the model the northward excursion of the SACCF as stated in *Orsi et al.* [1995].

III.3.4 500 meter isotherm tracked fronts

Front locations based on the temperature at 500 m (Fig. 10) are similar to those from surface elevation. The pattern of changes with different transport are the same as above. The fronts in the middle of Drake Passage tend to move northward with higher transport. The PF and SACCF deflect northward after passing the seamounts in the center of the passage. However, the frontal location based on temperature were more variable near the eastern boundary, especially for SACCF and SAF. These differences are due to eddy-induced spreading of the temperature. On the whole, there is a little difference between the frontal location determined by SSH or temperature at 500 m, indicating little difference between the surface and subsurface expression of these fronts. *Dong et al.* [2006] point out that the PF subsurface locations are a bit southward of the surface expression.

The SAF location is less variable and tends to shift northward with larger transport. In the smaller transport cases, the SAF forms a persistent meander east of the tip of South America and remains south of its historical location.

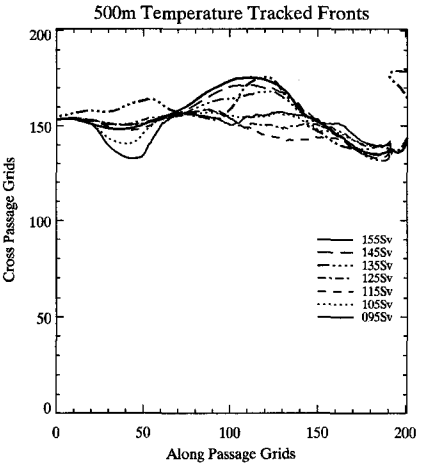

(a) Subantarctic Front

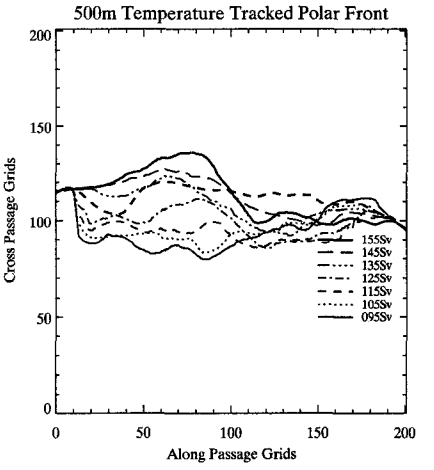

(b) Polar Front

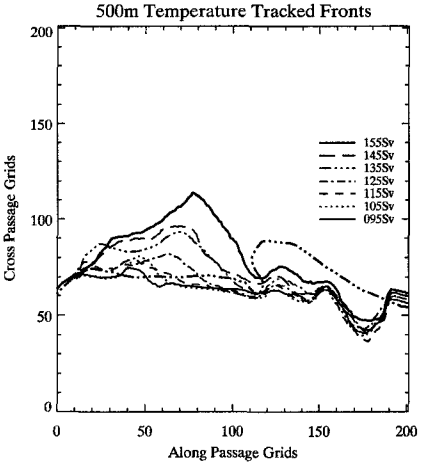

(c) Southern ACC Front

FIG. 10: Frontal location based on temperature at 500 m. The thick dash-dotted line is the historical location of the fronts.

III.3.5 Time series of isotherm locations from the ISOS moorings

Analysis of the ISOS moored temperature data indicated that the 2.0°C isotherm at 500 m was associated with the PF [*Hofmann and Whitworth*, 1985]. In the model, the 2.3°C isotherm is associated with the axis of the PF at the western model boundary. This small temperature difference is due to the Gaussian fronts in the model being based on averaged temperature and salinity in the zones between fronts. Though the 2°C isotherm was used as the indicator of the fronts at 500 m, it may not be consistent with the exact PF locations (maximum temperature gradient at the same depth).

The meridional location of the 2.3°C isotherm at 500 m in the model at the location of the ISOS main line along with the 2.0°C isotherm from observations are shown in Fig. 11. The simulated PF shifts northward with increasing transport which is consistent with the other indicators of PF location. For the smaller transport cases, the PF tends to move southward with time. For larger transport cases, the PF moves northward. At this location, the simulated PF is associated with meso-scale eddies, although the number of eddies declines as the transport increases. The observed location of the PF at the ISOS main line (Fig. 11h) is variable with no trend or seasonal pattern. Two PF eddies are observed in the 14 months of this record.

The model results have a somewhat different character from the observations. Each case displays a few small eddies along with large meanders of the PF. In the larger transport cases, the number of eddies is reduced over the smaller transport cases.

There are some irregular eddies occurring with a time scale of one to two months. These eddies may not be fully resolved since the grid spacing is close to the radius of deformation in southern Drake Passage. However, we find that the meandering of the SACCF did affect the path of the PF in Drake Passage. In other tests with shifted locations of the fronts, we see eddies moving northward (figures not shown). This northward motion pushes the PF northward for the larger transport cases. The northward meander of the PF pushes the SAF farther north. Thus, eddy generation from SACCF may be important for the overall character of the flow in Drake Passage.

Further discussion of the frontal location variations will be given in the discussion section.

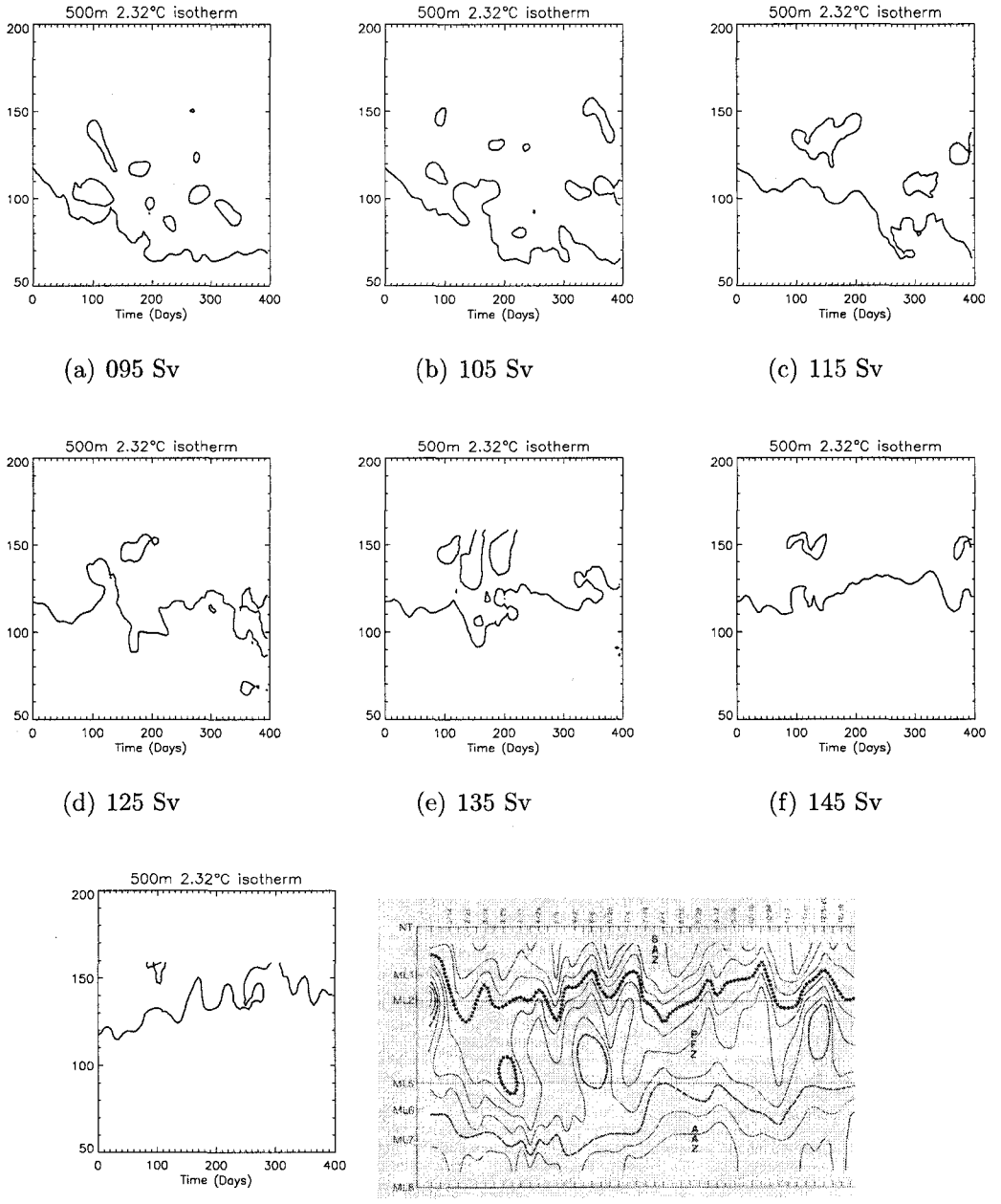

(a) 095 Sv (b) 105 Sv (c) 115 Sv

(d) 125 Sv (e) 135 Sv (f) 145 Sv

(g) 155 Sv (h) ISOS PF location

FIG. 11: Location of the Polar Front along model index $i = 80$. The location is close to the ISOS mooring main line, based on temperature at 500 m. The 2.32°C isotherm locates the PF in the model solution. Figure (g) is the PF locations from *Hofmann and Whitworth* [1985]. The 2°C isotherm is used to locate the PF in their study.

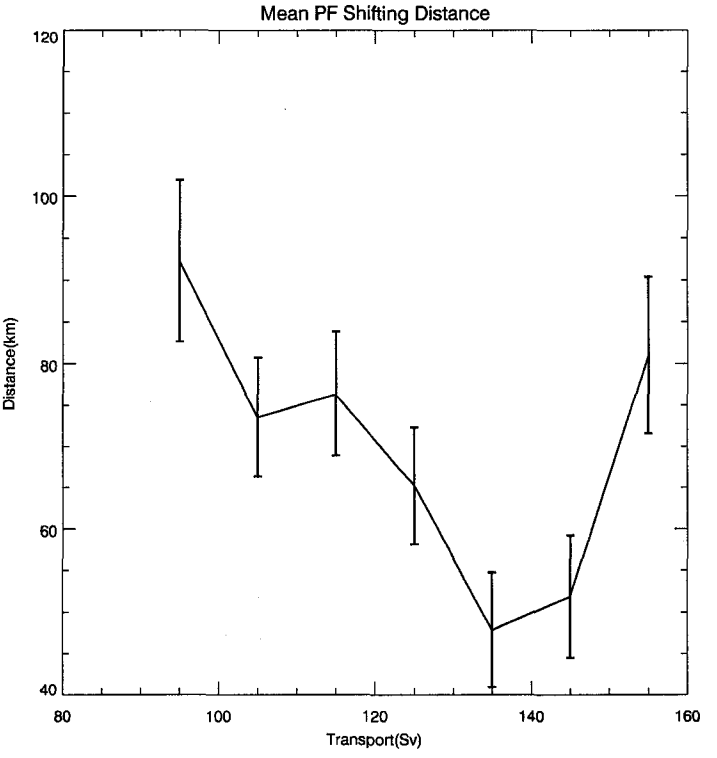

FIG. 12: Mean displacement of the Polar Front from its historical location for different values of imposed transport.

III.3.6 The effect of transport variation on the shifting distance of the PF

Different total transport affects frontal variability as well as the mean location of the fronts. The shifting distance of the fronts from their climatological location is a good diagnostic of the frontal variability. Among all the transport cases, the shifting distance for the PF is smallest (Fig. 12) with 135 Sv. The PF front is closest to the climatological location for this transport case. The PF shifts northward for increasing transport, and southward for decreased transport. The shifting distance also increases for other transport cases.

There is a fine balance between the baroclinic transport based on the model density structure (which is specified from WOA98 climatology) and the imposed barotropic speed at the western boundary (which sets the total volume transport), which controls the dynamic stability of the frontal jets. For the case with 135 Sv, the model

deviates the least from the observed frontal locations. This case might show the least conversion between the potential energy from the initial density structure and the total kinetic energy through the geostrophic adjustment. So that the PF doesn't need to adjust itself much to the imposed transport (135 Sv). For other transport cases, the PF may have to release potential energy (by flattening the pycnocline) or store potential energy (by tilting of pycnocline and becomes narrower), change itself in width and location to match the specified transport.

III.3.7 Ertel potential vorticity analysis

We choose the most realistic (135 Sv) case to calculate the EPV and transport streamfunction. The analysis time is day 390 which is close to the end of the simulation and the model has adjusted from the initial and imposed boundary conditions (other times late in the simulation yield comparable results). EPV is calculated at a variety of depths.

The relationship between EPV at 1500 m and the transport stream function (Fig. 13a) is clearly linear at most points. The correlation between EPV at different depths and the streamfunction (Fig. 13b) indicates that away from the surface and bottom, there is clear relationship. Theoretical analysis of EPV shows it should be conserved along streamlines in the absence of diffusion [*Gill*, 1982]. The maximum regression coefficient (more than 0.90) occurs for depths from 1000 m to 2500 m.

Between the surface and 750 m, the correlation changes from -1 to +1. Surface processes associated with strong flow shear and mixing (the effect of the KPP turbulence scheme) near the surface change the relationship between EPV and streamfunction. Similarly, within 500 m of the bottom, there is a reduction in this correlation which is due to the influence of variable bottom topography. Flow distortion by bathymetry and increased mixing reduces the conservation of EPV along streamlines.

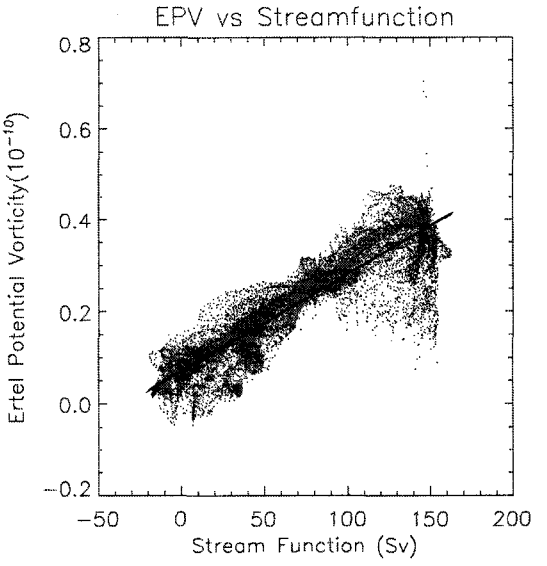

(a) Scatter Plotting of EPV and Stream Function

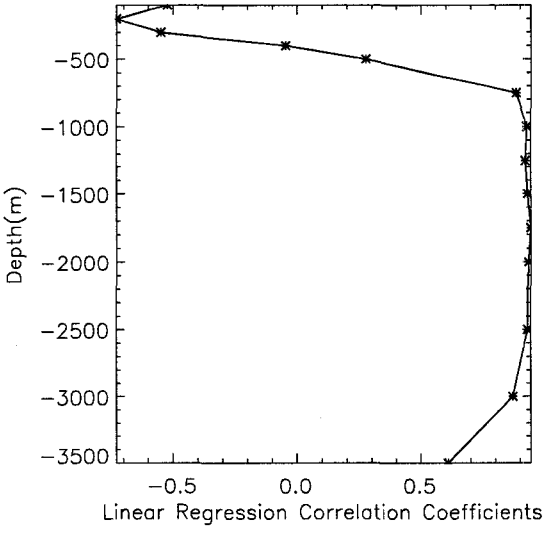

(b) EPV and Stream Function Correlation Coefficient with Depth

FIG. 13: The relationship between Ertel potential vorticity and streamfunction for 135 Sv at day 390.

III.4 DISCUSSION

III.4.1 Model realism

Sea surface elevation from satellite altimeters (provide by AVISO) provides a good test for these model solutions. The SAF is portrayed more realistically in the model compared to other fronts. The PF and SACCF shift northward in the model after passing the seamount area; a behavior that is observed on occasion. The model PF is wider downstream of the seamounts, which indicates greater variability in response to the variable bottom topography. Satellite observations portray the PF as several filaments rather than a single jet in the model snapshots. In any case, the averaged PF is wide and not easily distinguished in the mean SSH fields.

The SACCF in the model does not show the strong S meander near the Shackelton Fracture Zone. There are several possible causes for this inconsistency. First, the model resolution may not be fine enough to represent all of the features of this bottom topography. The model ridge is not as tall as the real ridge. In addition, in the southern Drake Passage the grid spacing is about equal to the internal deformation radius, so the dynamics may not be fully resolved. Second, there is no source of cold water from the western Weddell Sea which would have some influence on the meander near the tip of the Antarctic Peninsula. Finally, the southward deflection of the PF in some simulations can limit the northward excursion of the SACCF, reducing the effect of the topographically induced meander.

The PF location correspondence to the net baroclinic transport is reported in the SR-1 hydrography by *Cunningham et al.* [2003]. Along the SR-1 hydrographic section, the PF is in its southerly location for years 1993 and 1996 with the small net baroclinic transport (132 Sv); the PF is in its northerly position during years 1994, 1997 and 1999 with the large transport (142 Sv). Though this relation does not hold for year 2000 and this section is downstream of our model domain, it partially supports our results that the total ACC transport affects frontal locations.

There are several factors responsible for the different frontal locations for different imposed transport. The partition of the total transport among the frontal jets is proportional to the vertically integrated baroclinic transport. Thus, the changing transport is proportionally distributed among the three jets and the intervening zones.

The mechanism for the ACC transport changes in Drake Passage have not been identified, other than the commonly held opinion that the barotropic transport is the part that changes. The amount of transport change for the different jets has not been analyzed. Allowing the transport change to be accomodated by the SAF or PF alone is likely to lead to different results due to the stability of the SAF and the instability of the PF. These variations are beyond the scope of the present study, in particular because there is no observational evidence to guide these experiments.

III.4.2 Potential vorticity

Conservation of potential vorticity is used to explain the shifting of frontal locations with changing transport. For this analysis, the barotropic form of potential vorticity is used, or $q = \frac{\zeta+f}{h}$, where ζ is the vertical component of relative vorticity, and h is the water depth. Due to the weak stratification of the Southern Ocean, bottom topography has a strong effect on the flow. While vertical structure of frontal jets does exist [*Klinck*, 1985], surface elevation and the 500 m temperature fronts both give consistent locations for the fronts. The ACC fronts have the signatures through the water column [*Cunningham et al.*, 2003; *Orsi et al.*, 1995]. For simplicity, the discussion considers the frontal positions and meanders to be barotropic. The velocity here is vertically integrated velocity, the barotropic velocity.

The frontal jet is symmetric about its axis, so $\frac{\partial u}{\partial y}|_{x=0} \sim 0$ in the core of the jet. For a jet without a meander, which is the initial state, ζ in the jet center is near zero. Thus, the initial potential vorticity $q = f/h$, and the flow will follow planetary vorticity contours. The value for q to be conserved for each streamline is set at the western model boundary, where the water is deep. Assuming conservation of q, the relative vorticity in the model interior is $\zeta{=}q \cdot h - f$. In the Southern Ocean f is negative, so a decrease in depth leads to an increase in ζ.

Central Drake Passage has a depth around 3000 m and is shallower than the eastern Pacific Ocean with depths around 4500 m (in the model domain). This shoaling will generate positive relative vorticity which is consistent with a northward curvature of the frontal axis. The shoaling of Drake Passage makes the frontal jets shift to the north.

An alternative explanation for the northward frontal shifts is seen in the surface elevation (Fig. 6). The SACCF deflects northward (as meanders) after passing the seamount area in the southern passage leading to a northward shift of the PF. Eddies from the SACCF into the Antarctic Zone (the Zone between the PF and the SACCF) may have the same influence. Similarly, the PF may shift to the north affecting the SAF.

Fronts located by surface elevation or the 500 m temperature are consistent. Without local surface forcing in this regional model or variations of the boundary input, the surface temperature and salinity are conserved following the flow. The strong gradient in density and the longitudinal velocity maximum coincide in the vicinity of a developed front [*Gill*, 1982].

III.4.3 Model adjustment to initial conditions

The development of the PF jet occurs in two parts. First, the imposed jet assumes a quasi-geostrophic balance with the initial density at a time scale of $1/f$ (about a day). The gravity (barotropic) adjustment takes less than one day to set up the surface elevation according to the geopotential anomaly from the density structure. However, for a mean surface velocity of about 0.5 m/s, information at the western boundary will take about one month to cross the whole model domain (1200 km).

The second adjustment is due to diffusion caused by eddies and sub-grid scale mixing; generally, slow processes. The geostrophic frontal jet can become dynamically unstable (depending on flow speed and density structure). For strong enough flow, the developing mesoscale eddies can be swept downstream before they can pinch off. With smaller transport, the baroclinic instability is effective in releasing potential energy to form eddies and meanders. The observed PF location along the ISOS mooring line (Fig. 9h) appears less variable with large measured transport.

Stability of the SAF seems a different matter, which is changed fundamentally by the continental slope along the northern Drake Passage. Topography can stabilize flow or it can limit the size of the developing instability and halt its development [*Sutyrin et al.*, 2001]. The SAF is influenced by the topographic ridge just west of Cape Horn which allows the development of lee eddies under appropriate inflow

conditions. A hint of this influence is seen in the historical front locations (Fig. 2) and to some extent in the mean surface elevation (Fig. 6a).

III.4.4 Transport and Frontal Stability

Given the balance of kinetic and potential energy in the frontal jets, each front may only have a narrow range of imposed transport that is associated with realistic behavior. The SAF is narrow and strong with 155 Sv transport, while the PF is closest to its historical location at a transport of 135 Sv. The SACCF shrinks unrealistically to the south and is less variable with large imposed transport.

The structure and strength of the imposed transport and velocity structure are important for a short-term (several months) forecasting with regional meso-scale models. Furthermore, the flow paths of some frontal jets in the interior of this model have unrealistic meanders. This effect is most clearly seen in the surface elevation for smaller transport cases (Fig. 6(b)-(h)) where a southward meander develops in the SAF and the PF close to the western boundary. This meander is not evident as the transport increases.

III.5 CONCLUSIONS

These model results show a number of effects with different imposed volume transport. The varibility of ACC fronts in Drake Passage is clearly related to the volume transport of the ACC. With large transport, the SAF and PF spawn fewer eddies and therefore are more stable. The SAF, PF and SACCF shift northward with increased transport while they remain to the south with smaller transport. With smaller transport, the SAF develops large meanders. The transport and the frontal variability reflect the competition between the frontal available potential energy and the kinetic energy. Consistency of input transport and the density fields is important for regional mesoscale circulation models.

In all the transport cases, the mean shifting distance of PF from its historical locations is from 50 km to 90 km, which is close to the estimate (70 km) by *Gille and Kelly* [1996]. The minimum shifting distance occurs at a transport of 135 Sv,

which is consistent with the ISOS estimation to the total ACC transport of 134 Sv [*Whitworth*, 1983].

The SAF and SACCF are confined by northern and southern walls, respectively. The path of the PF is loosely controlled by the topography. After passing the seamounts in the central Drake Passage, the PF meanders strongly and becomes a wider flow.

The EPV is linearly correlated with the transport streamfunction between depths of 1500 meter to 2500 meter with a correlation of more than 0.9. Near-bottom flow has a weaker correlation between EPV and streamfunction. Near the surface, the correlation is weaker and even reverses sign. The smaller coefficient is caused by the removal of potential vorticity through friction and mixing, which are much larger near the bottom and the surface than those in the middle depths.

III.6 ACKNOWLEDGMENTS

The altimeter products were produced by Ssalto/Duacs and distributed by Aviso, with support from CNES. Computer facilities and support were provided by the Commonwealth Center for Coastal Physical Oceanography at Old Dominion University. We appreciate this support.

CHAPTER IV

WIND EFFECTS ON FRONTAL VARIABILITY

IV.1 INTRODUCTION

The Antarctic Circumpolar Current (ACC) circling the earth in the Southern Ocean is a wind-driven current. The wind stress is primarily balanced by form drag due to large variation of the bottom topography [*Nowlin and Klinck*, 1986; *Rintoul et al.*, 2001]. There are many arguments about form drag theory and Sverdrup balance [*Warren et al.*, 1996; *Hughes*, 1997]. *Warren et al.* [1996] revised the Sverdup balance theory proposed by [*Stommel*, 1957] that ACC is just like the subtropical gyre, which gains vorticity from the wind stress on the way circling the Antarctic and releases the vorticity in the Drake Passage area as a return circulation. Thus the wind stress curl should determine the ACC transport and is not related to the form drag. In circulation models of the Southern Ocean the form drag indeed is the primary balance of wind stress in zonal integration [*Gille*, 1997; *Jackson et al.*, 2006].

A simple review for form drag theory in the literature may help understand its importance in the Southern Ocean. The momentum balance in the model x (approximately zonal) direction is considered:

$$\frac{\partial u}{\partial t}+\frac{\partial u^2}{\partial x}+\frac{\partial uv}{\partial y}+\frac{\partial uw}{\partial z}-fv=-\frac{1}{\rho}\frac{\partial P}{\partial x}+\frac{\partial \tau}{\partial z}+D \tag{23}$$

where description of each variable can be found in Table 3.

The vertical integration of equation 23 gives:

$$\begin{aligned}\frac{\partial}{\partial t}\int_{-h}^{\eta} u dz+\int_{-h}^{\eta}\frac{\partial u^2}{\partial x}dz+\int_{-h}^{\eta}\frac{\partial uv}{\partial y}dz+u(\eta)w(\eta)-u(-h)w(-h)-f\int_{-h}^{\eta} v dz \\ =-\frac{1}{\rho}\int_{-h}^{\eta}\frac{\partial P}{\partial x}dz+\tau(\eta)-\tau(-h)+\int_{-h}^{\eta} D dz\end{aligned} \tag{24}$$

Furthermore,

$$\begin{aligned}-\int_{-h}^{\eta}\frac{\partial P}{\partial x}dz=-\frac{\partial}{\partial x}\int_{-h}^{\eta} P dz+P_b\frac{\partial h}{\partial x} \\ \text{where } P_b=P(z=-h)\end{aligned} \tag{25}$$

Variable	Description
u,v,w	(x,y,z) component horizontal direction velocity
f	Coriolis parameter
P	Pressure
τ_x, τ_y	(x,y) component of wind stress
D	Mixing terms
η	Surface elevation
h	Bottom depth
ρ	In situ density
P_b	Bottom pressure

TABLE 3: The variables used in momentum equation and induction of form drag.

In the Southern Ocean form drag theory [*Hughes*, 1997; *Warren et al.*, 1996], bottom friction, nonlinear terms and mixing terms are neglected. Thus, averaging over time,

$$-\rho f \int_{-h}^{\eta} v dz = -\frac{\partial}{\partial x} \int_{-h}^{\eta} P dz + P_b \frac{\partial h}{\partial x} + \tau(\eta) \tag{26}$$

The Coriolis term becomes zero for a circumpolar integration along a continuous latitude line (constant f) through Drake Passage due to volume conservation. The part involving the horizontal gradient of vertically integrated pressure (VIPG) becomes zero in a circumpolar integration. So the wind stress integration is only balanced by the form drag (the bottom pressure times the topography slope), the second term on the RHS on the equation 26. This balance can be expressed as:

$$0 = \oint \frac{1}{\rho} P_b \frac{\partial h}{\partial x} dx + \oint \tau dx \tag{27}$$

As the narrow choke point in the ACC pathway, Drake Passage provides large form drag due to the abrupt topographical change and the ACC directly hitting the walls when coming into the passage. Though the form drag has been calculated in the whole Southern Ocean in different models, there is no calculation of the form drag in a regional area. The comparison of form drag and wind stress in Drake Passage has not been demonstrated. It is necessary to evaluate the form stress at certain places in Drake Passage to better understand the local dynamics.

As the core contribution to transport and isopycnal tilting, the variability of the three ACC fronts must be affected by the wind stress, locally or remotely (through

upstream transport changes) and the form stress when encountering large changes in topography.

Kamenkovich [2005] analyzed the effect of different frequency wind stress on the surface mixed layer depth in a coarse resolution (2 degree) model. Daily wind stress has a large impact on the depth of the mixed layer and surface temperature structure in the Southern Ocean than that in the tropical ocean. This implies the high frequency wind stress might affect the frontal variability in the Southern Ocean since the Southern Ocean fronts can also be located from the surface temperature.

The wind stress in the Southern Ocean has considerable variability on a broad set of time scales [*Gille*, 2005]. With frequent storms, the strong surface wind stress may disrupt the mesoscale and sub-mesoscale surface circulation patterns and the upper layer temperature structure and thus, affect the northward motion of cold Antarctic Surface water. It is likely that the PF locations are affected by the strong wind forcing. Many studies have looked at the Southern Ocean response to the wind stress [*Gille et al.*, 2001; *Weijer and Gille*, 2005].

Peterson [1988] showed that at sub-seasonal time scales, the net transport is dominated by the barotropic activity. *Hughes et al.* [1999] found that the ACC variability is dominated by the barotropic mode (Southern Mode) driven by winds at periods between 10 days and 220 days. *Weijer and Gille* [2005] used an unstratified Southern Ocean model with a large range of high frequency wind stress with synoptic time scales to analyze the effect of wind stress on the transport variations. For time scales longer than a week, the free Southern Mode dominates the transport variability with an explicit wind-transport relation. For shorter time scales, the oscillatory modes are dominant. The Southern Mode usually follows the f/h contours, which are interrupted in areas of large abrupt topography, such as the Scotia Ridge [*Hughes et al.*, 1999].

Previous studies have found variations of the ACC in Drake Passage with time scales of one to three months. ISOS observations demonstrated the deep temperature (at 2700 m) fluctuates with a time scale of approximately two to three months [*Hofmann and Whitworth*, 1985]. *Gille and Kelly* [1996] showed that the PF variability has a time scale of 30 days. *Sprintall* [2003] also found that eddies from XBT and altimetry data have a time scale of 35 days. However, these sub-seasonal time scale

features in Drake Passage have not been fully explored and explained dynamically.

Dong et al. [2006] analyzed the relationship between PF locations (from surface SST gradient) and the Southern Ocean wind stress. They found that the tendency of the PF to shift coincides with the tendency of the longitudinal maximum wind stress to shift. This might explain some PF variations due to the wind stress. However, further examination of the wind stress and frontal variability is needed. It is not clear if this response is due to the dominant barotropic mode on the scales discussed in *Hughes et al.* [1999] and *Weijer and Gille* [2005].

Usually the large scale barotropic variability and the local baroclinic variability are difficult to separate in local observations [*Hughes et al.*, 1999]. What causes the sub-seasonal scale variations in Drake Passage is not clear and needs investigation either from a model or from completely synoptic measurements of hydrography and forcing. Due to the lack of the synoptic information from hydrographic survey and sparse resolution for concurrent measurements (ADCP, etc), a representative regional model with climate forcing is necessary to study realistic frontal scenarios.

Our purpose here is to look at the response of the PF variability in Drake Passage to the local wind stress and to find the time scales at which the wind stress is related to frontal variations. The relationship between form drag and local wind stress is also analyzed to characterize the contribution of form drag in regional ocean circulation dynamics.

In Chapter 3, the upstream total transport effects on the three frontal locations have been elaborated. This implicitly gives the remote (or whole Southern Ocean) wind stress effect on front locations. The local wind stress effects on the circulation and fronts were not considered. In this chapter, a regional frontal model is set up and different wind stress is specified in the model to see how the wind stress affects frontal locations.

In this chapter, the results from three model cases are analyzed: without wind stress, with 6 hourly unsmoothed wind stress (including the high frequency component, hereafter called 6 hourly wind stress) and with monthly running mean wind stress (low passed and is still 6 hourly data, hereafter called smooth wind stress). First, the surface and 500 m PF locations with different conditions are compared. The correlation between the wind stress, surface elevation and PF locations are then

examined. Finally, form drag in the model is assessed to illustrate its role in the ACC dynamics.

IV.2 MODEL CONFIGURATION

The model grids and topography are the same as in Chapter 3 except that the Shackleton Fracture Zone is enhanced by adding a Gaussian barrier, with the depth close to the correct value. The mixing schemes are the same as in Chapter 3: KPP vertical mixing and harmonic horizontal diffusion and viscosity.

In an attempt to test the wind stress effects, monthly wind stress [*Trenberth et al.*, 1996] is applied on the frontal feature model in Chapter 3 (135 Sv) for the first year. The PF locations show little difference with or without wind stress. To further examine wind stress effects, experiments with strong and mild wind stress (6 hourly and smooth wind stress (QSCAT/NCEP)) are carried out after the model runs a long time, usually 4 years. However, to set up a more realistic regional ocean model and dynamically adjusted model state over a longer simulation time, the initial conditions and boundary conditions are a little different from those in Chapter 3.

IV.2.1 Initial conditions

Hydrographic data from two cruises are used to set the initial conditions. Two CTD section measurements are chosen, because they are separated in space, and the frontal structure is clear. The first CTD data set is from hydrographic stations near the end of January, 1990, on the western side of the Drake Passage (WOA98 cruise number 8042). The second data set is from November, 1996 along the WOCE SR01 line close to the eastern side of Drake Passage. For most of the depths, the patterns of temperature and salinity are similar along these two sections. However at the bottom, the cold bottom water intrudes from the Weddell Sea on the eastern side, so the bottom water is colder and saltier than that on the western side.

First, the hydrographic data from the western cruise (8042) are examined. Each front is defined from the thermocline gradient as in *Orsi et al.* [1995]. Two CTD casts bracketing the SAF, the PF and the SACCF are extracted to use in setting

Gaussian type fronts. These data are mapped to the historical fronts using an error function to the line in the model closest to the measured CTD cast. In the mapping, an optimal method is used to keep the first order derivatives continuous, so that a smooth T/S profile is obtained. The mapped frontal width is the same as in Chapter 3. In doing that, elongating or shrinking the isotherm and isohaline a bit is needed to match the historical frontal locations. The same method is applied to the east side CTD hydrography and a mapped T/S profile is obtained on one vertical section of the model grid. Vertical extrapolation is needed when the model station is deeper than the real station.

Close to the western and eastern side of the model domain, two T/S profiles with frontal features between the historical SAF and the SACCF are obtained. The major differences between the two profiles are the bottom and surface temperatures. A simple linear relation between T/S and distance along the frontal axis at each depth is applied. Using this method, most of the water mass characteristics in Drake Passage are unmodified; therefore, the vertical stratification and the horizontal gradient in the model initial conditions to the north of SACCF are more realistic.

Water properties on the slope and coastal areas south of the SACCF and the north of SAF also need specifying. Hydrography measurements exist in the Bransfield Strait and WAP almost concurrently with the cross-passage CTD cruise (8042). An optimal interpolation method is applied to blend the coastal observations and the frontal initial data from methods above. This blending requires special treatments in setting up the vertical temperature and salinity profile where the measured depth is less than the model station depth. Vertical extrapolation and horizontal interpolation need careful treatments to obtain reasonable T/S condition and stable stratification. To the north of SAF, the observations from the western CTD cruise in that area are mapped to the east and north of SAF. In the Powell Basin, observations from an adjacent area with the same depth and close in time (seasonally) for different years are included, so that some cold water is enforced along the southern boundary. Thus, the model includes the Antarctic Bottom waters on the eastern side of Drake Passage, coastal waters (cold) in the WAP, and the slope waters along the continental slope on the model area of the Powell Basin.

The initial temperature is shown in Fig. 14. There is a relatively smooth temperature field in the vertical profile and relatively warm water on the surface, as it is

astral summer when the CTD profiles were taken.

IV.2.2 Boundary conditions

The geostrophic velocity is calculated from the initial conditions referred to the lowest common depth as in Chapter 3. The total input transport is specified along the western boundary as 135 Sv. The transport structure along the boundaries are simply increased to match the total transport.

In the south, based on the Deep Ocean VEntilation Through Antarctic Intermediate Layers (DOVETAIL) observations, analytical 2D velocity is specified based on the flow directions along the tip of the WAP and in the Powell Basin. This analytical flow is given as a qualitative function of mean temperature and topography. The total northward transport is about 5 Sv and the southward transport is 4 Sv. The 1 Sv transport is assumed to go westward to join the transport in Bransfield Strait. The northern boundary is weak in its dynamical effect and has little effect on the ACC fronts. Therefore, the northern boundary to simplify the model geometry is set to be closed. To keep the volume conserved in the model, the input transport through the southern boundary and the western boundary match the total transport out of the eastern boundary.

The regional model prevents us from using any periodic boundary conditions. So we used methods similar to those proposed by *Marchesiello et al.* [2001]. The hydrography (initial conditions) is strongly relaxed along the open boundaries. The nudging time scale is gradually reduced to infinity over the 10 points (approximately 60 km) at the boundary. For outflow, smaller nudging coefficients are applied so that eddies can propagate out. A sponge layer (10 points wide) is applied along the eastern boundary. With these boundary conditions, the model runs for several years to a dynamically balanced steady state, where the volume averaged total kinetic energy reaches to a stationary steady state.

IV.2.3 Forcing conditions

Blended wind stress from QuickSCAT satellite and National Centers for Environmental Prediction (NCEP) reanalysis [*Milliff et al.*, 2004] is used to calculate the surface

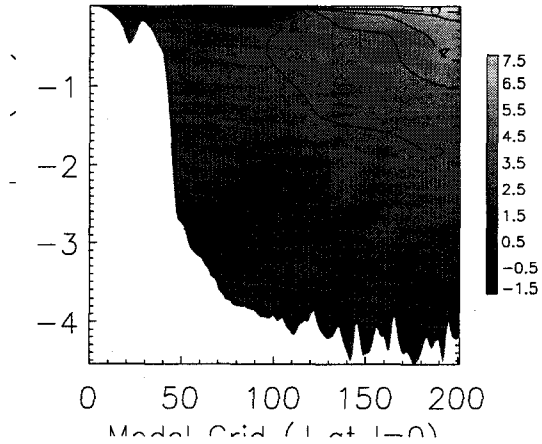

(a) Initial temperature along the model's western boundary, looked toward west

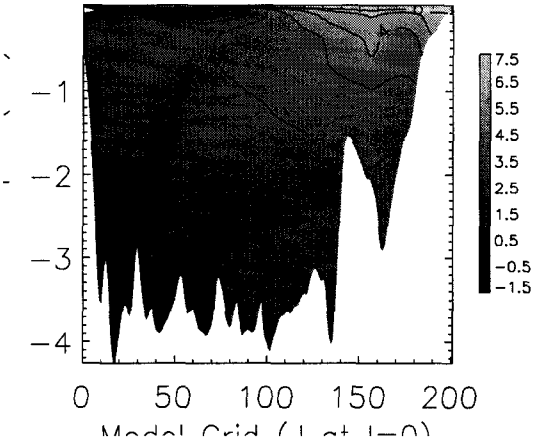

(b) Initial temperature along the model's eastern boundary, looked toward west

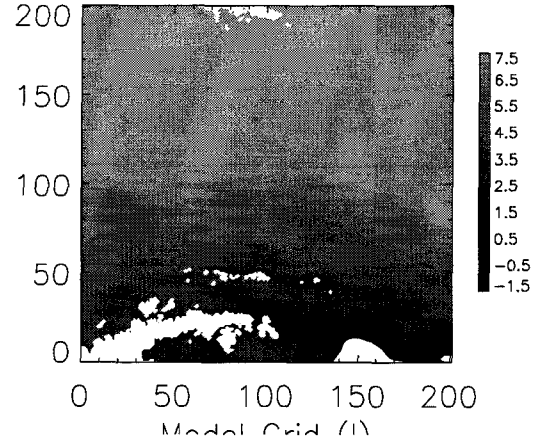

(c) Initial surface temperature in the model

FIG. 14: The initial temperature in the model. Color bars and contour lines both indicate the temperature. The eastern bottom temperature is colder than that at the western side.

wind forcing. A simple conversion of the wind velocity to the wind stress is accomplished with (*http://www.cora.nwra.com/~morzel/blendedwinds.qscat.dirth.2002.html*):

$$\begin{aligned} \vec{\tau}_s &= \rho_a C_d |\vec{u}| \vec{u} \\ C_d &= 0.00118, \quad when\ |\vec{u}| \leq\ 10m/s \\ C_d &= 0.00049 + 0.000069 \times |\vec{u}|, \quad when\ |\vec{u}| \geq\ 10m/s \end{aligned}$$

where $\vec{u}$ is the wind vector at a height of 10 m, C_d is the neutral 10 m drag coefficient, and ρ_a is a typical air density. The QSCAT/NCEP wind data set has $0.5^o \times 0.5^o$ and 6 hourly resolution. The calculated wind stress is linearly interpolated to the model grid. The smooth wind stress is created with a 30-day running mean applied to the interpolated 6 hourly wind stress.

A quadratic bottom stress is used as a function of the bottom velocity $\vec{u}$: $\vec{\tau}_b = \rho C_b |\vec{u}| \vec{u}$, where C_b=0.003 is the drag coefficient and ρ is the bottom sea water density.

IV.2.4 Model cases

The model is run for 4 years without wind stress to let the temperature and salinity fully adjust to the boundary conditions and the topography. During the fifth year, the surface forcing is added. Three model cases are considered: the 6 hourly wind stress, the smooth wind stress and zero wind stress.

IV.3 ANALYSIS METHODS

IV.3.1 Analysis of terms in the momentum equation

Due to its importance in balancing the Southern Ocean wind stress, form drag in numerical models is often calculated through the integration of the momentum equation along a circumpolar latitudinal line [*Gille*, 1997; *Jackson et al.*, 2006]. There is no closed latitudinal line in the regional ocean model over which to take the integration. Integration along any chosen path may introduce additional pressure errors when the ending depth is not equal to the starting depth. A general calculation method and form drag mechanism of blocking the current are discussed in *Edwards et al.* [2004].

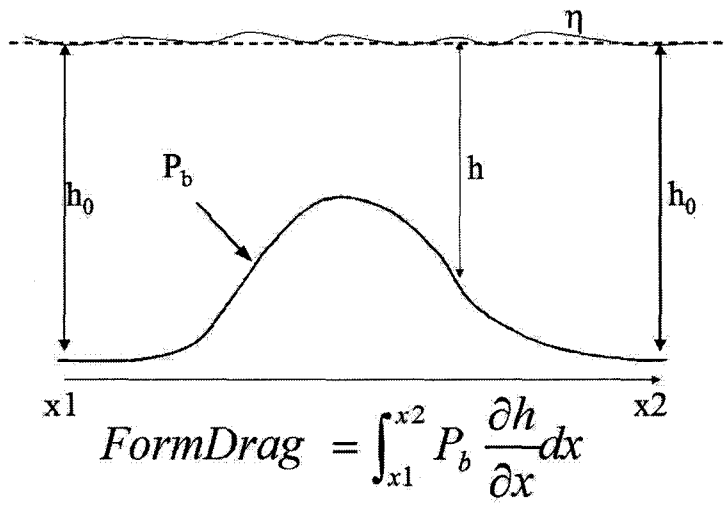

FIG. 15: Schematic plot of calculation of the form drag over a seamount. The starting and ending point must have the same depth.

The form drag $P_b \delta h$ has no meaning at a single point. Form drag represents the integrated effect of the topography. It must be integrated over an area or along a line covering topography. A schematic plot of form drag (in one direction) over a seamount is shown in Fig. 15.

Only x direction momentum equation in the model are considered. To simplify the calculation, several lines are chosen to make the calculation. Each line extends eastward in x direction from west boundary to an ending point, close to the eastern boundary, with the same depth as its starting point. To include as much as possible of the topography through this integration line, only the segment with a distance more than 150 grid points (approximately 900 km) is used. The eastern ends of the chosen segments are shown in Fig. 16.

The vertical integration of the momentum equations must be done along this line to evaluate the form drag. Direct calculation involves the pressure term which may cause large errors. A simplified calculation instead for the VIPG term is:

$$\begin{aligned} \nabla \int_{-h}^{\eta} P dz &= \nabla \int_{-h}^{\eta} \int_{z}^{\eta} \rho g dz' dz \\ &= \nabla \int_{-h}^{\eta} \int_{-z}^{\eta} \rho_0 g dz' dz + \nabla \int_{-h}^{\eta} \int_{-z}^{\eta} \rho' g dz' dz \end{aligned} \tag{28}$$

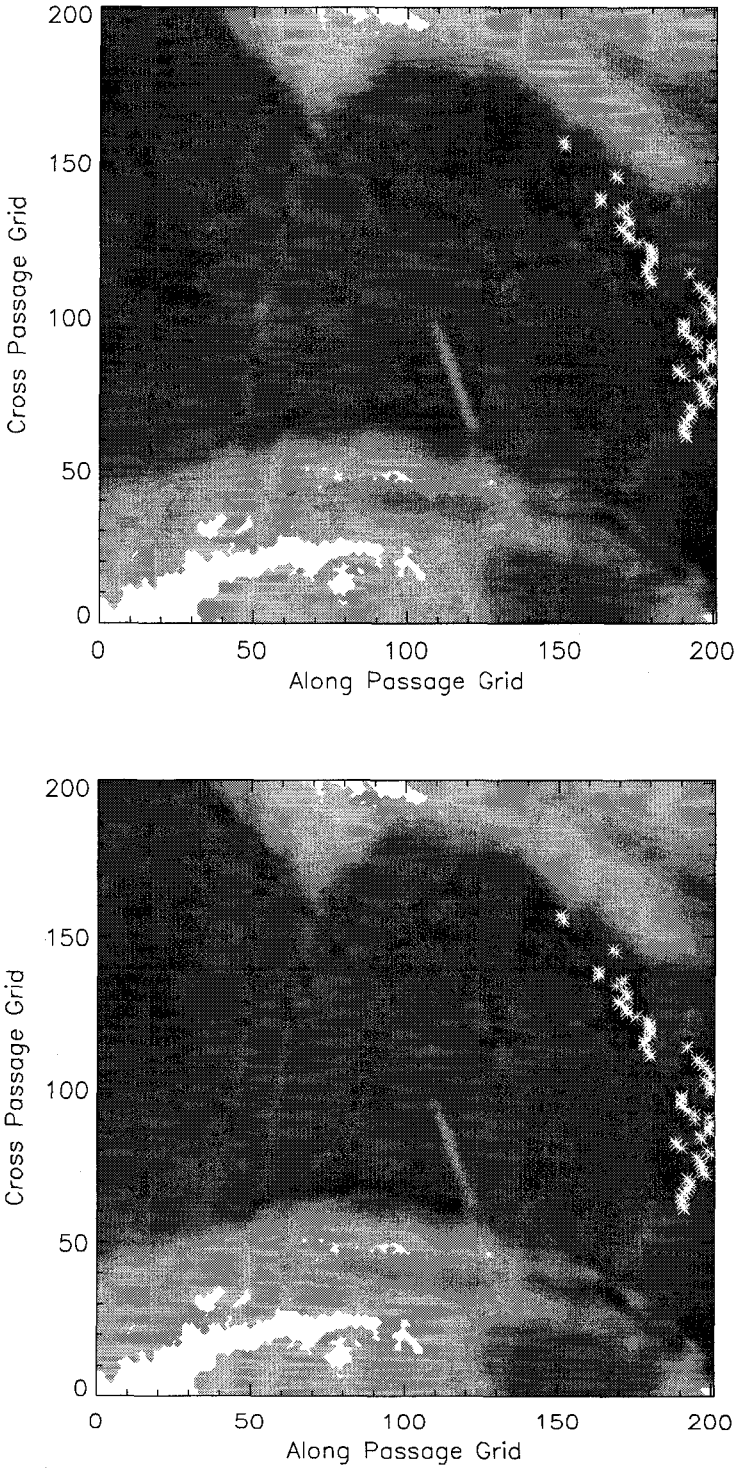

FIG. 16: Ending points of the lines where the form drag and momentum equation integration are carried on. The star indicates the ending point of each line. The starting points of these lines are on the western boundary. The starting point and end point have the same depth. The integration line is along x direction in the model. The shades show the topography roughly.

$$= \rho_0 g \nabla(\eta + h)^2/2 + \nabla \int_{-h}^{\eta} \int_{-z}^{\eta} \rho' g dz' dz$$

and for the form drag term is:

$$\begin{aligned} P_b \nabla h &= \int_{-h}^{\eta} \rho g dz \nabla h \\ &= \int_{-h}^{\eta} \rho_0 g dz \nabla h + \int_{-h}^{\eta} \rho' g dz \nabla h \\ &= \rho_0 g \nabla h^2/2 + \rho_0 g \eta \nabla h + \nabla h \int_{-h}^{\eta} \rho' g dz \end{aligned} \tag{29}$$

where z' is also vertical coordinate and $\rho' = \rho - \rho_0$. When calculating the form drag along a chosen line (horizontal integration along this line), the first term in the form drag is zero due to the equal depth between the start and end point, and can be omitted. The second term is due to the pressure from the surface elevation, and the third term is due to pressure from density perturbation. The latter two terms are not large numbers, and their horizontal integration can be more accurate than directly integrating the right terms in equation 29.

The vertical and horizontal integration of other terms in the momentum equation are relatively simple. First a vertical integration is taken. Then horizontal integration along the chosen line is carried out. For comparison, the integration terms are scaled with $h_0 \rho_0 L$, where h_0 is the water depth of the starting point, ρ_0 is the mean density, and L is the horizontal distance of the line. So finally each term from the integrated momentum equations has the same units as fv, which is on the order of $10^{-6} m/s^2$. Notice that the scaled fv term is not zero because integration is not along a line of constant f.

The integration is carried out for each recorded model state. The terms are time averaged for comparison of different model cases.

IV.3.2 Polar Front location

The PF can be tracked from the surface elevation as in Chapter 3. Along the western boundary, the front location is fixed and the surface height at the axis is almost constant over the whole simulation. The mean elevation used to track the front is approximately 0.08 m out of the surface elevation increase of 1.3 m from south to north. Using this method, isolated eddies or small rings are not counted as any part of the front.

For one year model results (the fifth year), the PF locations are recorded every 2.5 days providing 144 PF locations. Some of them have large S-shape meanders especially in the seamount region. The usual way to calculate the PF locations in such situations is to use the southernmost location [*Dong et al.*, 2006; *Moore et al.*, 1997]. This causes errors where eddies or rings are mistakenly counted as the front or when the front splits. To reconcile these errors, the frequency of PF passing by each model grid is calculated. The number of times the PF exists in each model grid for all 144 PF locations is given. Given the occurrence of the PF at each grid, estimates where the PF occurs most often, and where the PF never appears can be made. If there is constant splitting of PF or alternative constant path, it can also be seen in the distribution map. The variability of the PF to its mean location can also be easily seen in this way.

The PF can also be tracked from the 500 m temperature. The same calculation of the PF locations is made to look at the surface and subsurface difference of PF under the wind effects. The three model cases with different wind stress are considered and compared in the following section.

IV.4 MODEL RESULTS

IV.4.1 The evolution of the total volume averaged kinetic energy

The total volume averaged kinetic energy (Fig. 17) is not constant; however, the tendency to increase as seen in Chapter 3 ends before the fifth year. The oscillation and peaks in the VAKE reflects baroclinic activity and the open boundary effects [*Marchesiello et al.*, 2001]. The mean and standard deviation of VAKE before time t are shown to see if the VAKE reaches a stationary state (Fig. 17(b)). At the fifth year, the standard deviation variation is really small. However, the mean VAKE drops a little bit. The model state at the end of the fifth year is used as the initial condition for the wind stress simulations. Though the state variables are kept, the vertical mixing coefficient is recalculated in ROMS. This causes the drop of VAKE around day 1440. Overall, except these effects, the model has reached a dynamically steady state.

With different wind stress, the kinetic energy behaves differently. Over the model's

last year, where the wind stress is applied, the VAKE with smooth wind stress case is smaller than that with 6 hourly wind stress most of the time. This implies that the increasing variability in the model interior is due to storm impacts. In contrast, the VAKE without wind stress is more like the case with 6 hourly wind stress. The three cases have similar patterns (the peaks, the crests), which implies the wind stress impact may not be as strong as the inertial motion of the stream in developing flow instability in the interior. There is further discussion in the next section.

IV.4.2 Mean sea surface elevation

The mean surface elevation shows little differences among the three cases (Fig. 18). Different fronts in the mean surface height are clearly distinguished. The SAF lies at the north of the model domain with strong surface elevation increasing over a short distance along the north wall. To the south of SAF, the PF can be seen clearly from the surface gradient but weaker than that of SAF. The southernmost surface increase over a short distance is the SACCF, which is the weakest of the three fronts.

The mean surface elevation contours coincide for the three wind stress cases except some small scale variations. The PF splits when it passes over the seamount area. To the north, the loop (curvature) is strong. Part of the northern branch joins with the SAF and part of it goes back south to rejoin the PF. To the south, the branch is weak in the mean fields. In this PF splitting, the northern branch is strong and southern branch is weak.

The differences are clear in the fine structures of the sea surface height. Only the PF locations are compared to simplify this analysis. In the seamount area, the contour lines with same surface elevation value have different shape with different wind stress. For example, the 0 cm isoline is continuous when passing over the seamounts in the mean fields with smooth wind stress, while it breaks up to form eddy-like structures for the 6-hourly wind stress and no wind stress cases. The strength and width of the front (in the mean field) at the same places also changes with different wind stress.

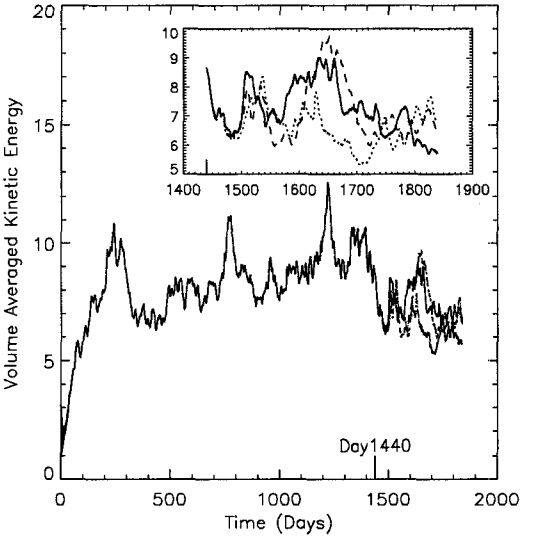

(a) VAKE

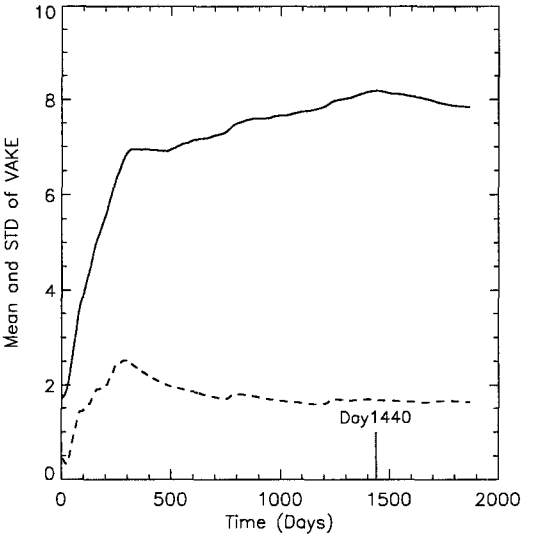

(b) Mean and STD of VAKE

FIG. 17: Total volume averaged kinetic energy and stationary test of VAKE. (a) The small box above is the expanded curves from day 1400. The solid, dotted and dashed lines represent the no wind, smooth wind and 6 hourly wind cases, respectively. The fifth year begins on the day 1440. (b) The stationary test for VAKE for 6 hourly wind stress case. The solid line represents mean of VAKE before time t. The dashed line represents the standard deviation of VAKE before time t.

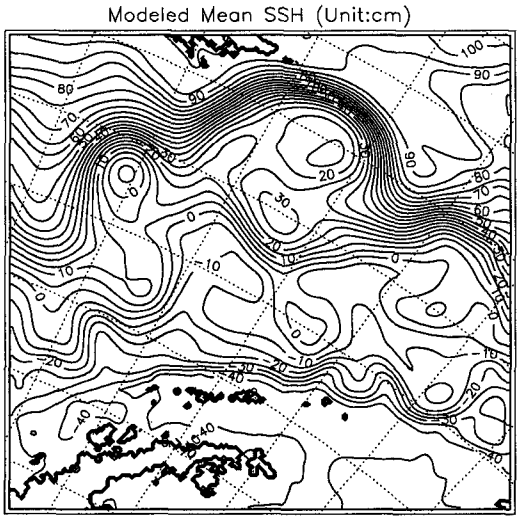

(a) Mean SSH for 6 hourly wind stress

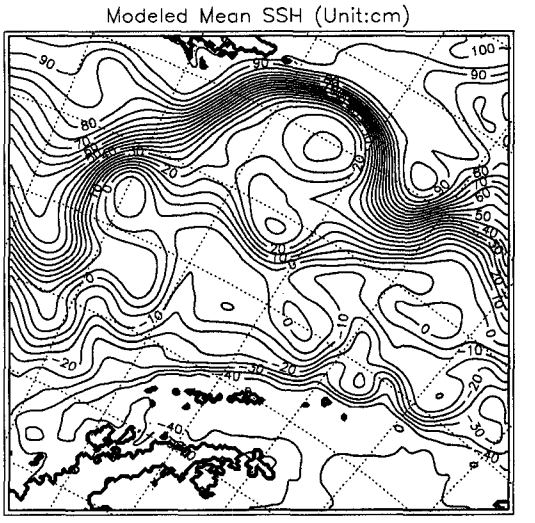

(b) Mean SSH for Smooth wind stress

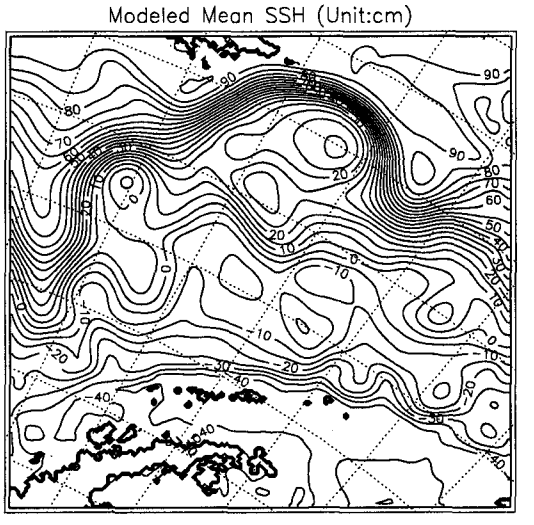

(c) Mean SSH without wind stress

FIG. 18: The mean sea surface height with different wind stress. The results are from the fifth year model surface elevation averaging

IV.4.3 Surface elevation statistical PF locations

The statistical PF locations in the model after long time integrations are clearly different in many places from the historical locations (Fig. 19). Although an expected PF location can be estimated from the frequency of the PF appearing at each grid points, it does not result in a monotonic function of x (not shown) due to the splitting or S meanders of the PF at some places. Most of the time the PF stays close to a fixed path. The large difference occurs in the seamount area, where the PF deflects away from the historical location. A big meander occurs between I direction grid point 50 to 100. Downstream of the big meander, the PF becomes zonal until close to the buffer boundary zone. But this path is still a bit north of the historical one.

In the surface elevation tracked PF locations, there is a very strong splitting of the PF before it encounters the seamounts. This feature appears in the mean sea surface height also (Fig. 18), where the strength of the northern and southern branches is not equal. With 6 hourly wind stress, the splitting is clear. With smooth wind stress, the splitting is not very clear and the PF stays to the north most of the time. For the no wind stress case, the PF stays mostly north and has no southward splitting at the seamount area. Splitting does not mean that the PF has two paths at the same time, but rather that the PF may follow either a southern or northern path.

To the north of the north end of the Shackleton Fracture zone, the distance of the modeled PF to the historical locations is the shortest for the case with 6 hourly wind stress, while the PF tends to stay north without the wind stress. The PF stays north up to the buffer zone, where the PF is forced back to its historical location on the eastern boundary.

Another remarkable feature is that at different places with different wind stress, the high occurrence of the PF (the dark region along the axis of the PF) appear with smooth wind stress. With the smooth wind stress, the PF is relatively stable (highest occurrence of PF appearing in some grid points close to the mean axis) while it is more variable with 6 hourly wind stress. In the seamount region, the graded area becomes thinner and less dark, which means the PF appears less frequently at given locations. However, the case without wind stress gives plausible results, and it shows a loose, less stable front than the smooth wind stress case.

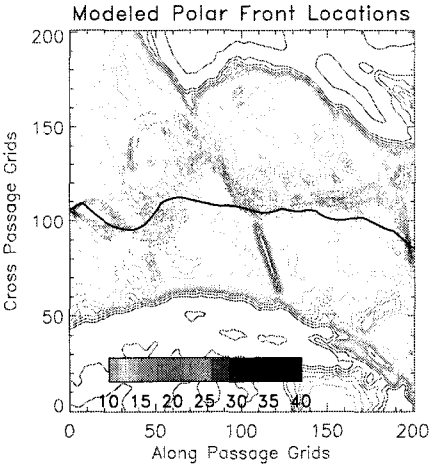

(a) PF Locations with 6 hourly wind stress

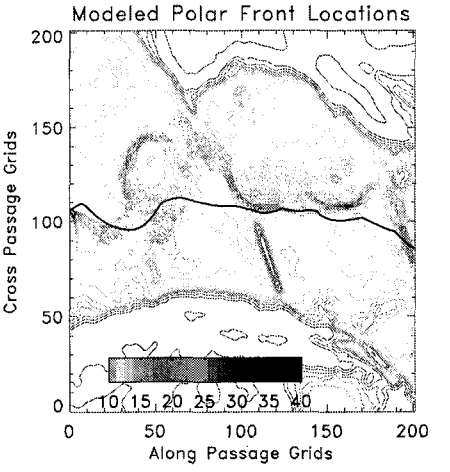

(b) PF Locations with smooth wind stress

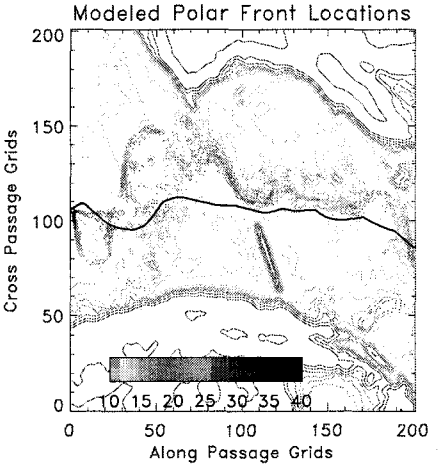

(c) PF Locations without wind stress

FIG. 19: The occurrence of the PF at each grid point with different wind stress. The black line is the historical PF location from Orsi et al. (1995). The color bar shows the occurrence of the PF appearing in each grid point over the last model year.

Close to the western boundary for the case without wind stress, the PF occurs in two different locations (between I index 0 and 30) (Fig. 19c). With wind stress forcing, this feature is weak (6 hourly wind stress) or disappears (smooth wind stress). This demonstrates that the different wind stress may affect the boundary conditions and the numerical errors from the boundary may contribute to the PF variability, especially when the wind or instability causes westward reverse flow or propagating waves.

IV.4.4 Time series of the surface elevation along several I index

Two places are chosen to look at the PF variations in the time series of surface elevation (Fig. 20): one is close to the seamount area (I index 50), the other is downstream of the ridge (I index 140). At the first location, the PF has large variations; while, at the downstream location, the PF is relatively stable.

In the I=50 time series, the PF to the north merges with the SAF. From the surface elevation it is difficult to tell which part is the PF. It is also difficult to separate the SACCF from the southern branch of the PF if there is part of the PF going south. There was no clear correlation between the wind stress amplitude and the PF variations in this area. However, at day 1530 and day 1750, two large eddies pinch off for the 6 hourly wind stress, while these features are not present in the smooth wind stress case.

In the I=140 time series, the PF can be detected from its strong horizontal gradient. The separation of three ACC fronts is clear, though the SAF seems to take most of the transport. The PF width changes with time, becoming narrower after day 1650. This feature is common for both wind stress cases. Another remarkable feature is the mesoscale eddies that pinched off from the SAF with a time scale of about 1 month, such as the ones at day 1570, 1650 in the 6 hourly wind stress case and at day 1640 in the smooth wind stress case. When an eddy propagates to the PF area, it helps to shrink the PF. In the case where two eddies enter into the same area (day 1640 with smooth wind stress), the PF becomes the narrowest. This might be related to the eddy-mean flow interactions, which the eddies can accelerate the front, though much debate on whether the eddies should decelerate or accelerate the front [*Hughes and Ash*, 2001].

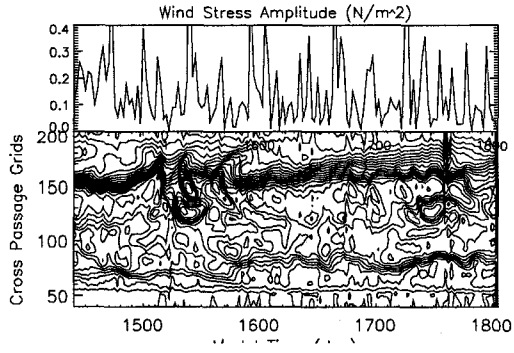

(a) Surface elevation at I=50 with 6 hourly winds

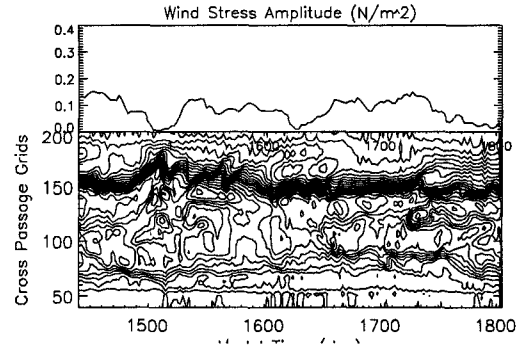

(b) Surface elevation at I=50 with smooth winds

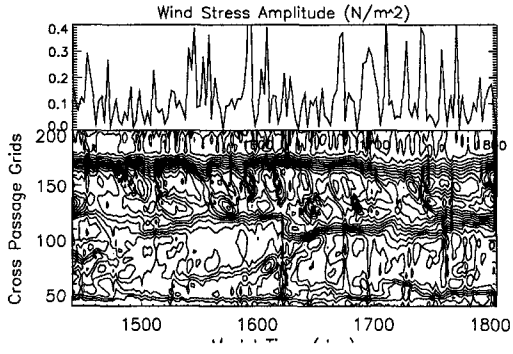

(c) Surface elevation at I=140 with 6 hourly winds

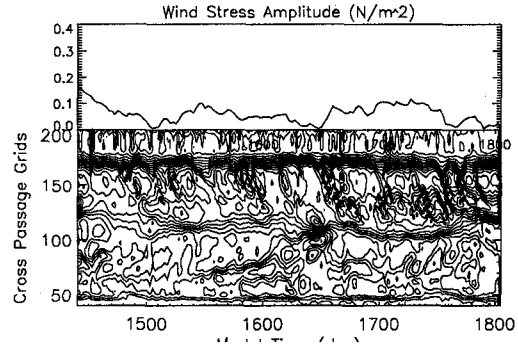

(d) Surface elevation at I=140 with smooth winds

FIG. 20: The surface elevation and wind stress amplitude time series at I index 50 and I index 140.

To closely examine the wind stress and front location effects, the smoothed wind stress and the surface elevations at four chosen grid points ((50,100), (50,150), (140,100), (140,150)) are plotted (Fig. 21). The U component of wind stress is generally larger than the V component. It is hard to see a direct response of surface elevation to the V component wind stress, while a direct response to the U wind stress is clear (Fig. 21). The surface elevation increases when the U component wind stress increases. This relation can be better seen in J=100 than J=150. This may imply that the SAF baroclinic instabilities in the northern PF exercise more control over the dynamics than regions south of the PF. To see at what time scale the wind stress affects the local variability, a cross correlation of wind stress and the surface elevation at these four points is examined.

IV.4.5 Cross correlation spectrum of sea surface height and the wind stress

Cross spectral analysis is done at the chosen locations for the sea surface variation with wind stress amplitude and direction to see how the wind stress affects the location of the fronts. Since the model state is recorded every 2.5 days, the interval of time for the cross correlation is 2.5 days. For one year of model results, only correlation with frequencies from half a year to several days are considered.

The cross correlation between the wind stress and the surface elevation is done for four locations. Two points for I=50 are considered where J=100 and J=150. Point at J=100 is close to the southern branches of PF (or SACCF). Point at J=150 is close to the northern branch of the PF (or SAF). For I=140, the analysis is done at J=150 and 100, so that they fall into zones between the PF and SAF, and between the PF and SACCF. Increasing elevation at the southern grid means that the PF moves south and vice versa.

The coherence between the wind stress and surface elevation at different locations shows similarities (Fig.22). There are several frequencies at which the coherence exceeds 0.5 and is above the 95% confident level. However, for different locations, the peak frequency is close but not the same. The spectra of U component wind stress and the surface elevation correlation at different locations are compared. At grid (140, 100), the peak values are 8 days and 30 days. At grid (140, 150), the peak

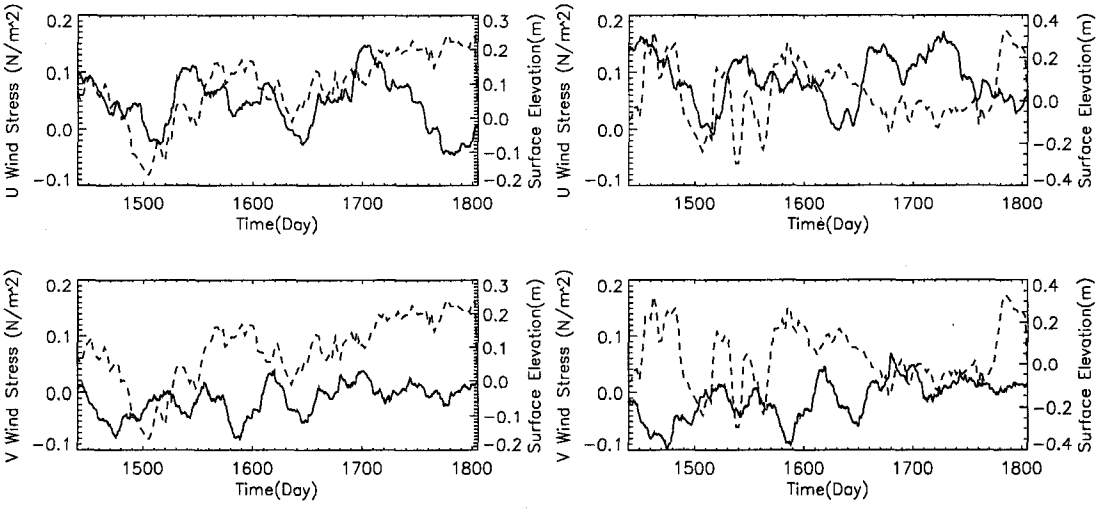

(a) Surface Elevation at (50,100) with 6 hourly winds

(b) Surface Elevation at (50,150) with 6 hourly winds

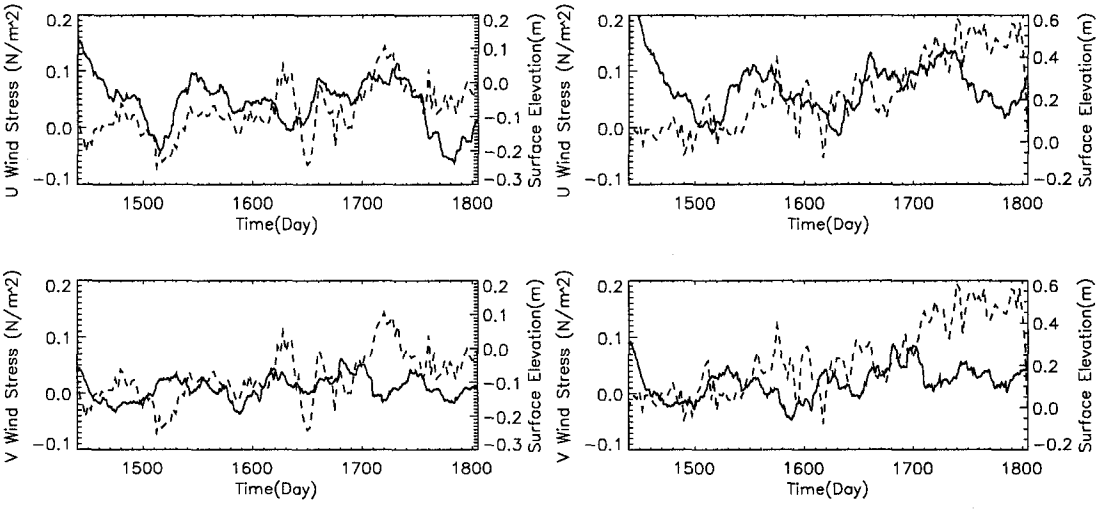

(c) Surface Elevation at (140,100) with 6 hourly winds

(d) Surface Elevation at (140,150) with 6 hourly winds

FIG. 21: The surface elevation (dashed line) and wind stress (solid line) time series at four grid points (50,100),(50,150),(140,100), (140,150). The U component wind stress shows the same patterns as the surface elevation, while the V component is less similar. Notice that the wind stress is applied after day 1440.

values are 8 days, 16 days and 40 days. At grid (50, 100), the peak values are 7.5 days and 30 days, though the coherency for the 7.5-day period is close to 0.5 while that at the 30-day period is 0.78. At grid (50,150), the peak values are 8 days, 14 days and 36 days. The largest differences occur between the south and north stations but not in the zonal direction. There is no feedback from the model to the wind stress fields. The wind stress should lead the surface elevation if they are correlated to each other, which means a negative phase lag in the spectrum analysis. Except at grid (50,150) and the 8 day period at grid (140,100), the phase lags are all negative at the peaks (Table.4), which shows the wind stress leads the surface elevation at the frequencies. Further discussion is given in the discussion section.

TABLE 4: The peak periods and according phase lag in the coherence spectrum between wind stress and the surface elevation at different locations. Both units are day.

location	(140, 100)	(140, 150)	(50, 100)	(50,150)
period/phase	8.0(3.3)	8.0(-0.5)	7.5(-3.3)	8.0(7.0)
period/phase		16.0(-6.8)		14.0(8.0)
period/phase	30.0(-10.0)	40.0(-31.0)	30.0(-21.0)	36.0(33.0)

IV.4.6 500 meter temperature tracked fronts

Dong et al. [2006] found that the surface PF tends to be south of the subsurface PF. In Chapter 3, without wind forcing, there is a difference between the PF surface and 500 m temperature tracked front locations. The subsurface PF is usually located from the subsurface temperature (such as the northern extent of 2 degree isotherm at 200 m as in *Dong et al.* [2006] and [*Sprintall*, 2003] or 500 m 2 degree isotherm). This relationship with wind stress is looked in this study.

The PF locations based on 500 m temperature are shown in Fig. 23. The patterns of the PF at 500 m look similar to those from surface elevations. The major paths of the surface and 500 m PF (dark area in the figure) coincide. The 500 m PF are more diffuse than from surface elevation (Fig. 19). Some features, such as the southern branch near the seamount area of PF with smooth wind stress becomes unclear. While the splitting of the PF at the same region with the 6 hourly wind stress is relatively

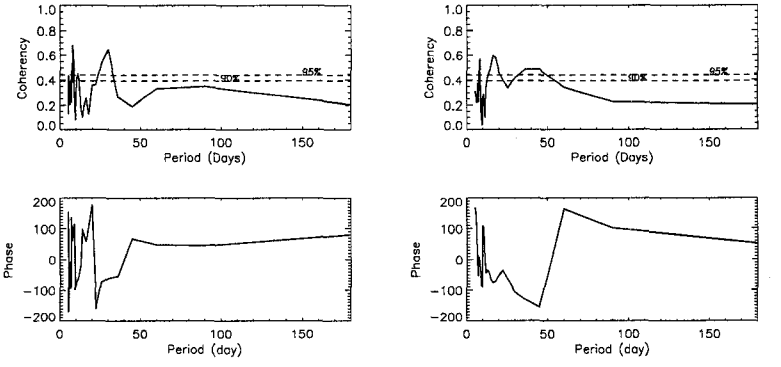

(a) I=140, J=100

(b) I=140, J=150

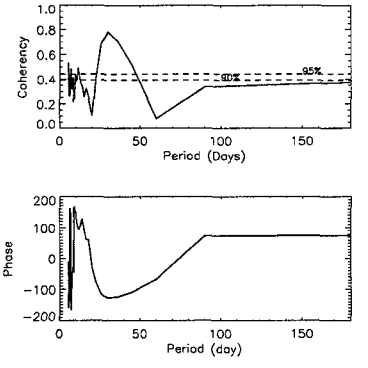

(c) I=50, J=100

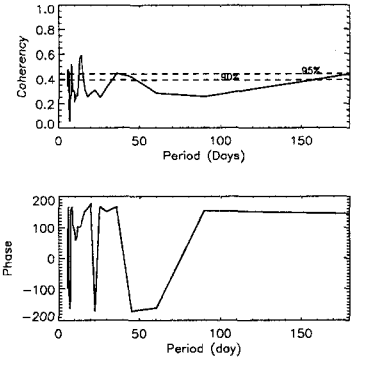

(d) I=50, J=150

FIG. 22: The cross spectrum of u component wind stress and sea surface height at four chosen grid points.

clear.

Direct comparison of the surface and subsurface frontal locations seems difficult from Fig. 23 and Fig. 19. The mean locations of the PF are calculated from the surface elevation and 500 m temperature as in chapter 3 (Fig. 24). When the PF has multiple locations, we use the southern most locations to calculate the mean PF location. The PF locations with different wind stresses are different. These differences vary with regions. Close to the western boundary the PF locations with no wind, smooth wind and 6 hourly wind stress are aligned from south to north. From I index 30 to 140, the relative locations reverse. The PF with 6 hourly wind goes to south, while the PF without wind stress lies to the north. Between 90 and 110, the PF with smooth wind is very close to that with 6 hourly wind stress. Downstream after I index 150, the PF without wind stress is southernmost, while the PF with 6 hourly wind stays in the middle until they merge to their common ending points on the eastern boundary. Similar patterns can be observed in the temperature tracked fronts (Fig. 24(b)).

The surface and subsurface PF locations are shown together for different wind stresses (Fig. 25). For all three cases, the surface PF location stays consistently to the south of the 500 m PF locations. This shows the local wind stress does not change the relative location of the surface and subsurface PF.

The maximum difference between the surface and 500 m PF locations occurs between I index 50-70, which is the region just upstream of the seamount area. This implies that bottom topography affects the relative position of the surface and subsurface location. *Dong et al.* [2006] compare subsurface and surface PF locations at Drake Passage and south of Australia, and find the distance between the surface and subsurface PF varies with seasons and locations. On the other hand, the maximum difference is different with different wind stress. The maximum difference is about 71 km for the 6 hourly wind stress, 80 km for smooth wind stress and 90 km for no wind stress.

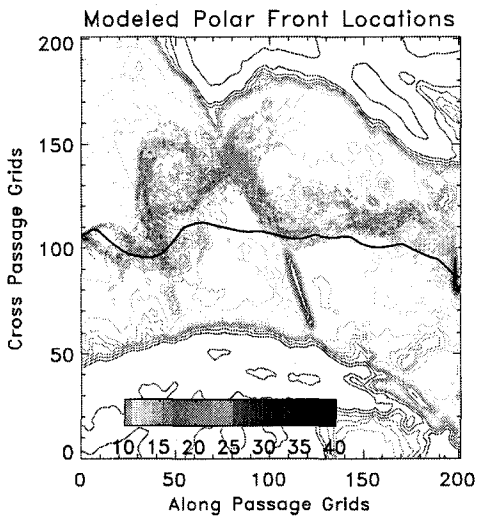

(a) 500 m PF with 6 hourly wind stress

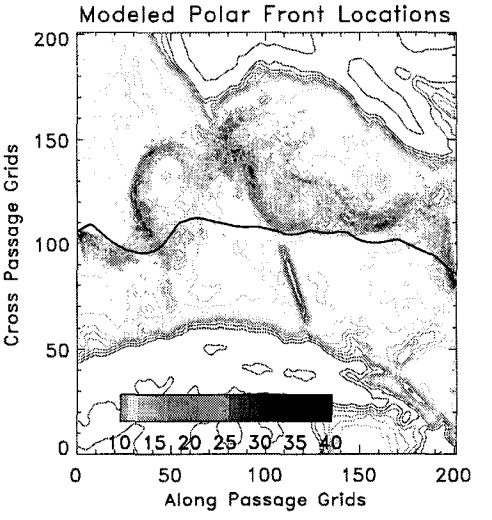

(b) 500 m PF with smooth wind stress

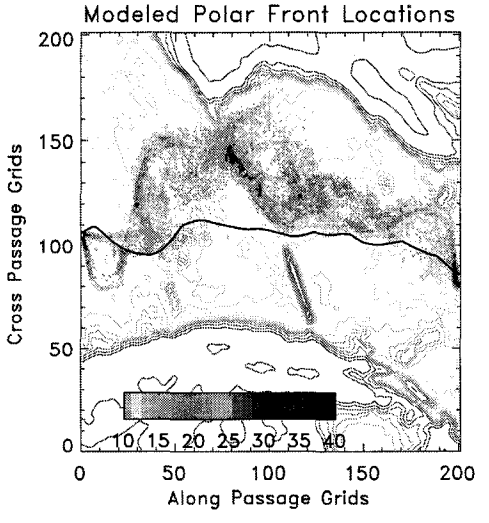

(c) 500 m PF without wind stress

FIG. 23: The PF location tracked from 500 m temperature.

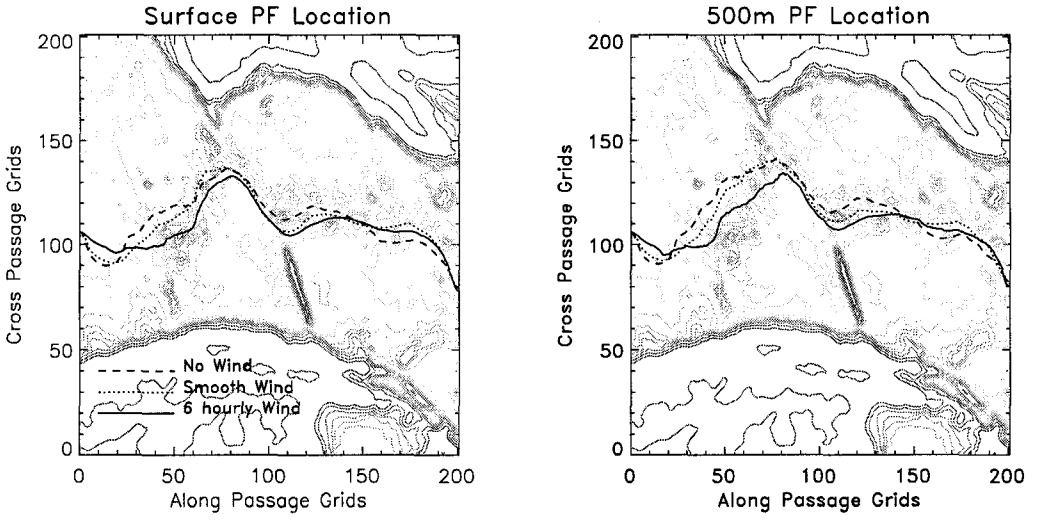

(a) Surface elevation tracked fronts

(b) 500 m temperature tracked fronts

FIG. 24: The mean PF location from surface elevation with different wind stress.

IV.4.7 Examination of the momentum equation balance

The vertical and zonal integration of the momentum equation along the chosen model grid lines are shown in Figs. 26 and 27. Be aware that due to the rotation of the model domain, the integration line is not along any line of constant f, but just a model grid line, thus the integration of fv term is not necessarily zero.

Not surprisingly, the major dynamics controlling the momentum balance in the model is the fv term and the vertical integration of the pressure gradient term (Fig. 26), which corresponds to the geostrophic balance. In the Southern Ocean, the circumpolar integration along a continuous latitude line of these two terms becomes zero above topography. Other terms in the momentum equation are looked at to assess their contributions.

Form drag is compared to the stress in Fig. 27. All three cases show large fluctuations of form drag with location. Large form drag is found where the abrupt change of topography occurs. The large form drag occurs at the Shackleton Fracture Zone (The ridge is aligned in the box of I index 100-120, J index 50-100). To the north of the ridge, there are several peaks (the positive values) in the form drag.

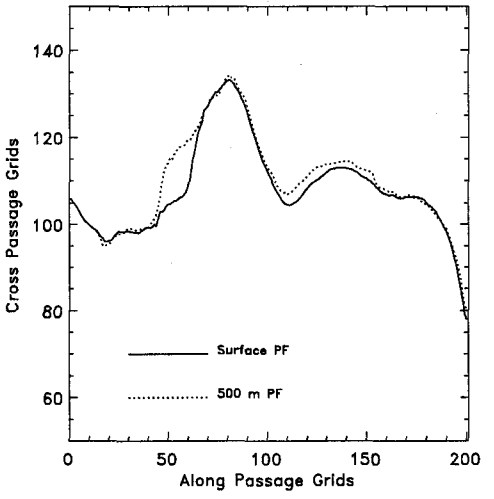

(a) 6 hourly wind

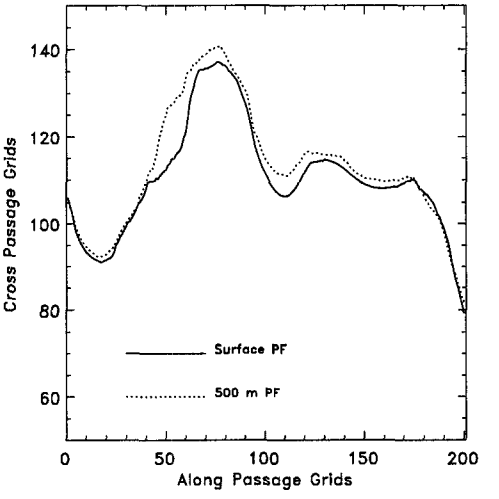

(b) Smooth wind

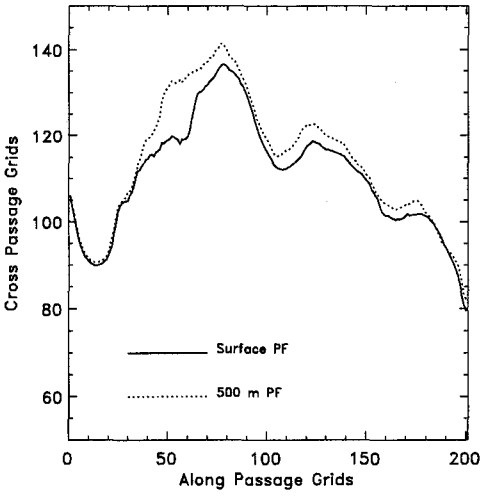

(c) No wind

FIG. 25: Surface and 500 m PF location comparison for different wind stress. The common feature is that the surface PF lies a little south of the 500 m PF.

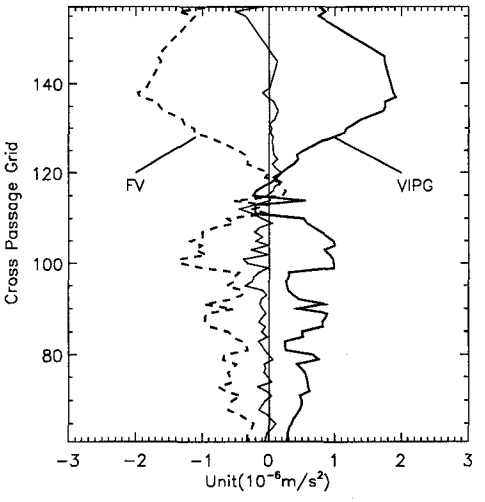

(a) FV and VIPG term for 6 hourly wind stress

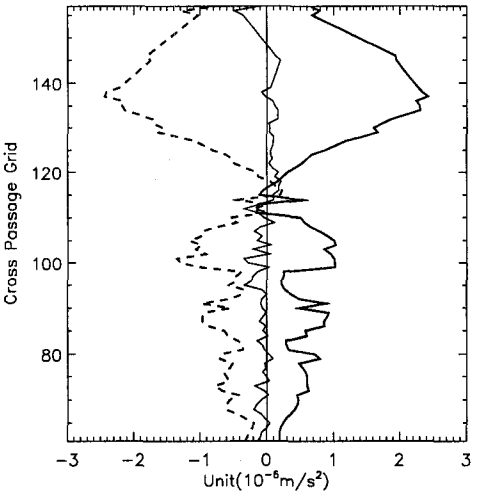

(b) FV and VIPG term for smooth wind stress

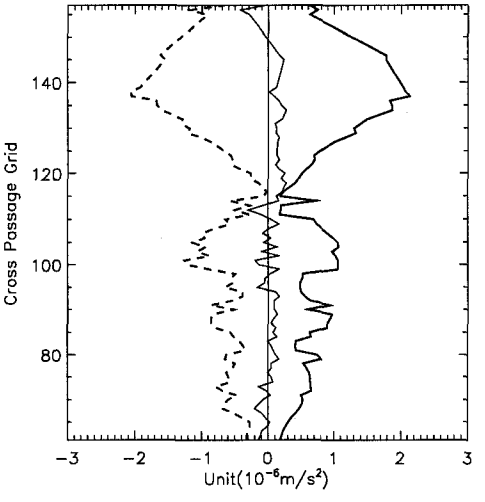

(c) FV and VIPG term for no wind stress

FIG. 26: The integration of fv and VIPG terms. All terms are scaled by $(h_0 \rho L_x)$. The difference of these two is shown as the solid line in the middle.

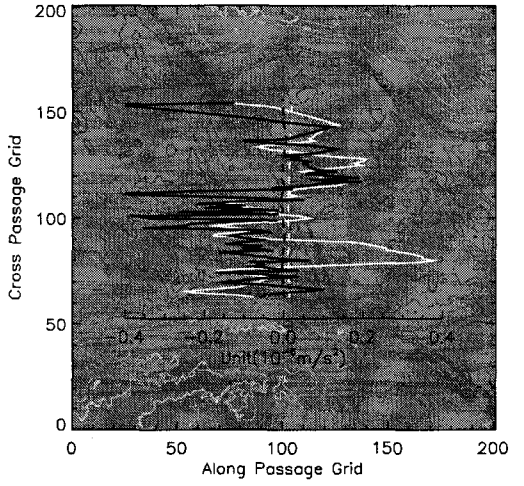

(a) Form Drag and Stress for 6 hourly wind stress

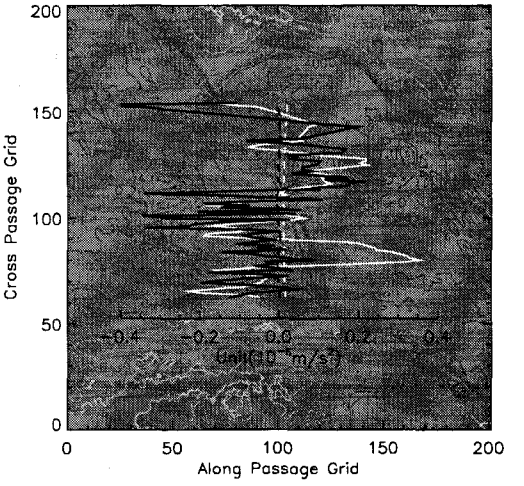

(b) Form Drag and Stress for smooth wind stress

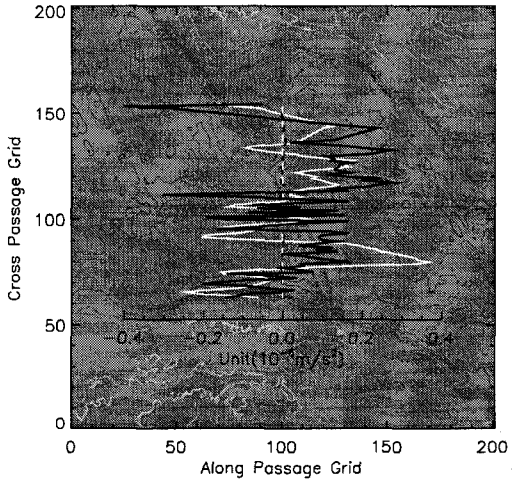

(c) Form Drag and Stress for no wind stress

FIG. 27: Integrated form drag, wind stress, bottom stress and FV-VIPG term. All terms are scaled by $h_0 \rho L_x$ and time averaged. The white solid line represents the form drag. The black solid line represents the FV-VIPG term. The dashed white line represents the wind stress. The black dashed line represents the bottom stress. A negative form drag slows down the eastward flow.

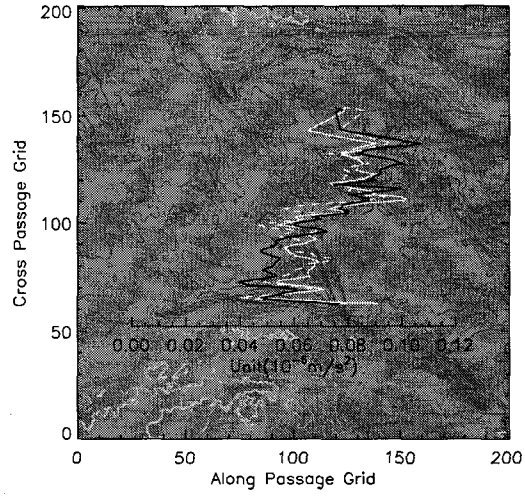

FIG. 28: Standard deviation of form drag with different wind stress. The white solid line represents the 6 hourly wind stress case. The white dashed line represents the smooth wind stress case. The black line represents no wind stress case.

These peaks correspond to groups of seamounts, though here the seamounts are not as sharp as portrayed in ETOPO2.

Variations of form drag (unit of fv) with topography are in the range of $-0.2 \sim 0.4\times10^{-6}m/s^2$, much larger than that of bottom stress τ_b and the wind stress τ_s. Even the integral of form drag along the y direction (cross-passage) for all the calculated values are more than two times larger than the integral of wind stress and two orders larger than the integral of bottom stress.

Comparing the three wind stress cases, we see only small differences in the structure of the mean form drag. Wind stress has a small effect compared to the specified transport, and the mean circulation structure in Drake Passage would not change much solely due to the local wind stress. The standard deviation of form drag with time (Fig. 28) is around $0.06\times10^{-6}m/s^2$ in the south (J=60 $\sim$ 100) and around $0.08\times10^{-6}m/s^2$ to the north of J=110. The difference of the standard deviation from different wind stresses is less than $0.02\times10^{-6}m/s^2$.

The advection terms are comparable to the form drag, while the three components of the advection are not equal (Fig. 30). In our calculations, the $\frac{\partial u^2}{\partial x}$ is negligible compared to other terms. The uv and uw terms are comparable to form drag, though

the errors caused from the uw term in cases with large slopes may be large due to the pressure gradient error.

The mixing and acceleration terms are also calculated (Fig. 29). For 6 hourly wind stress case, the vertical mixing has a mean value of $0.008\times10^{-6}m/s^2$, while horizontal mixing term has a mean value of $0.0002\times10^{-6}m/s^2$. The accelelation term has a value of $0.001\times10^{-6}m/s^2$. The vertical mixing term for no wind stress case is much smaller than that with wind stress. This is due to the KPP mixing with different wind stress cases. The summation of the mixing and acceleration terms are around one order smaller than the form drag term. This indicates that they have less contribution to balance the form drag.

As summary from the momentum balance, besides the basic geostrophic balance, the other important terms are the form drag and the nonlinear terms involving lateral and vertical shears. The wind stress, bottom stress, mixing and acceleration terms are small in this regional model compared to the form drag.

The summation of the momentum equation (Fig. 31) does not give a closed balance. The significant discrepancy occurs at large slope area. The calculation is done along the bottom, which is also an S coordinate surface (where $s = -1$). It involves the pressure term. There is an error which is similar to the pressure gradient error with vertical stratification and horizontal density gradient. The VIPG term includes double vertical integration of the pressure, which is a very large number. However, only its horizontal gradient is needed. This term might also bring large error in the integration of the momentum equation. At a coarse conclusion, the integration of fv term is close to the VIPG term, which are two dominant terms in the momentum equation. The form drag is large compared to the stress, nonlinear or the mixing term, while it is still much smaller compared to the fv terms. At the first order approximation, we can say the momentum equation is closed as the geostrophic balance. For the second order terms, the errors from integration involving pressure terms destroy the balance. However, the relative importance among these terms is still significant.

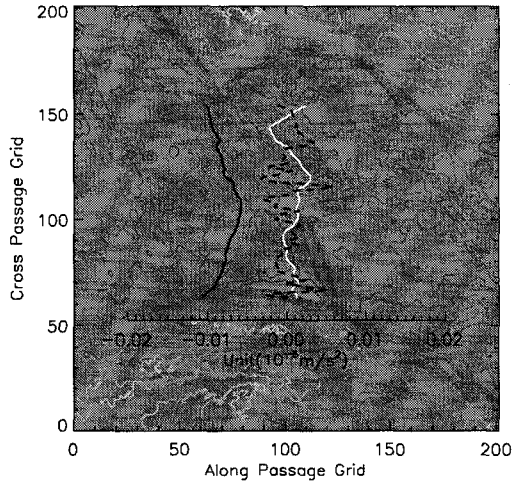

(a) Mixing terms for 6 hourly wind stress

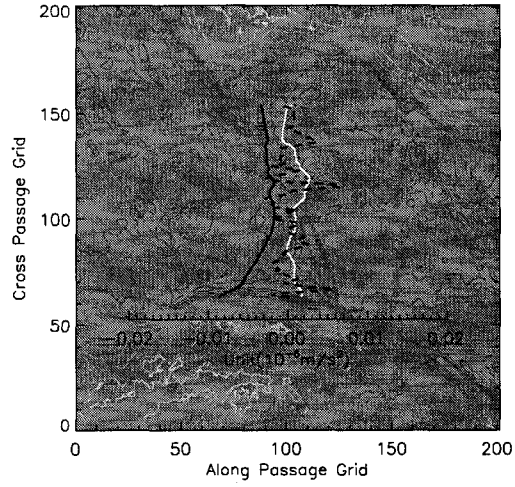

(b) Mixing terms for smooth wind stress

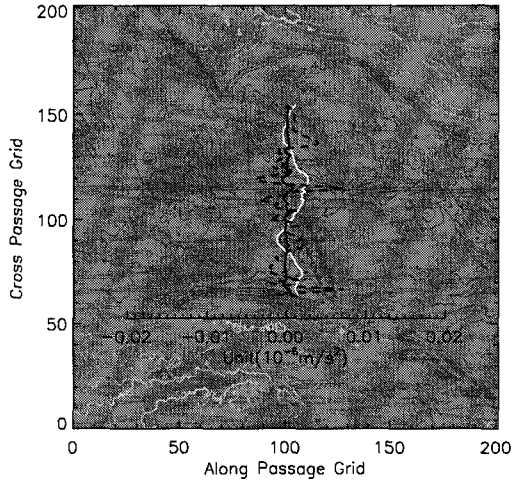

(c) Mixing terms for no wind stress

FIG. 29: Integrated mixing and acceleration terms. All terms are scaled by $h_0 \rho L_x$ and time averaged. The white solid line represents the acceleration term. The black dotted line represents horizontal mixing term. The black solid line represents the vertical mixing.

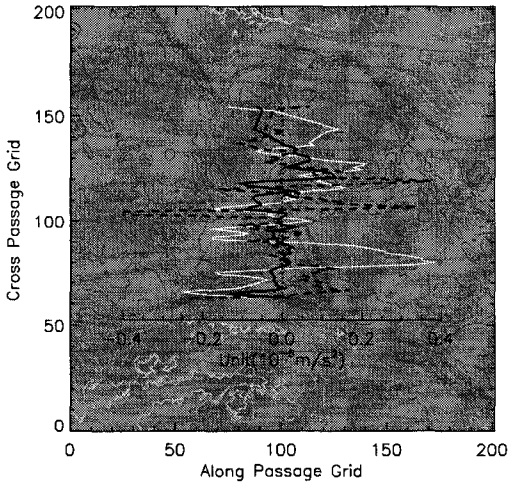

(a) Form Drag and Advection for 6 hourly wind stress

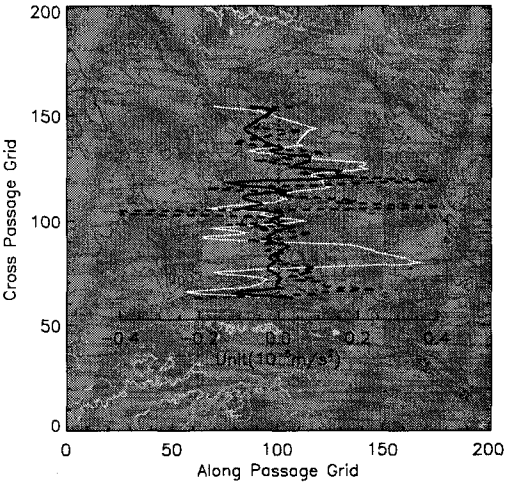

(b) Form Drag and Advection for smooth wind stress

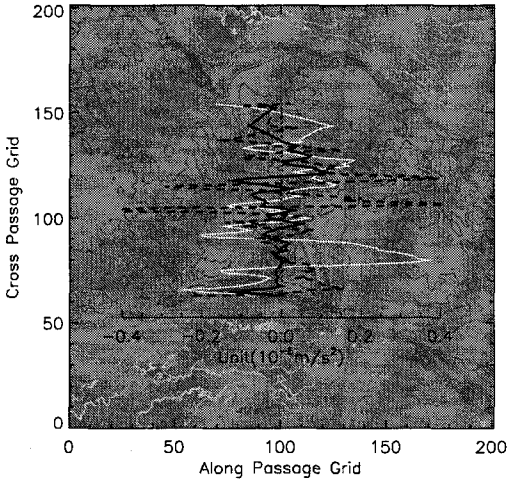

(c) Form Drag and Advection for no wind stress

FIG. 30: Integrated form drag and three advection terms. All terms are scaled by $h_0 \rho L_x$ and time averaged. The white solid line represents the form drag. The black dotted line represents the $\frac{\partial u^2}{\partial x}$ term. The black solid line represents the $\frac{\partial uv}{\partial y}$ term. The black dashed line represents $\frac{\partial uw}{\partial z}$ term.

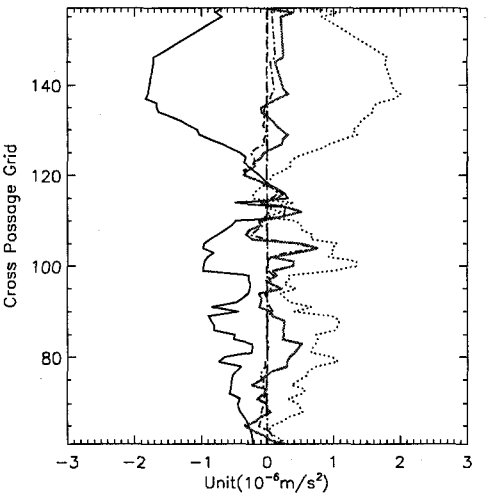

(a) 6 hourly wind stress

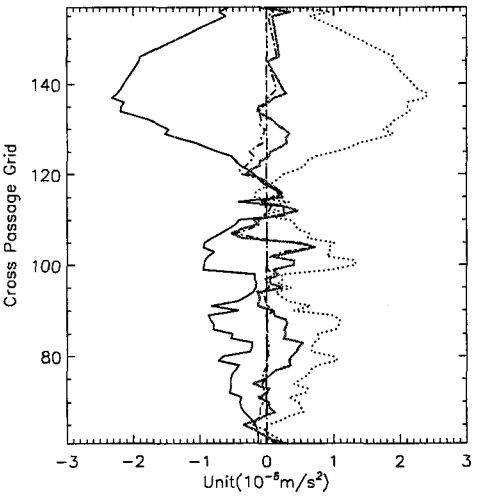

(b) smooth wind stress

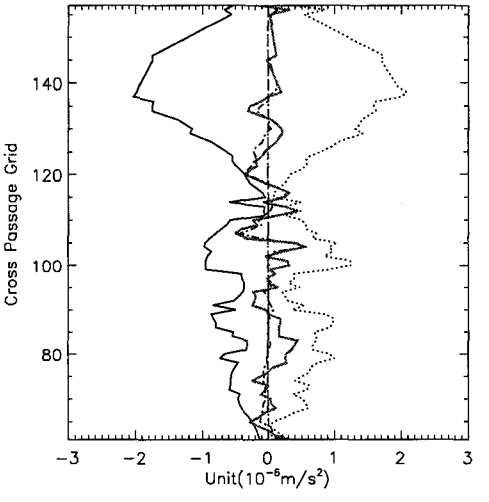

(c) no wind stress

FIG. 31: Examination of the balance of the integrated momentum equation. All terms are moved to the right side in eq. 23. The solid black line represents fv term. The dotted line represents the pressure gradient term (VIPG + Form Drag). The dash-dotted line represents all the nonlinear terms. The stress, mixing terms are very small and are not visible hidden behind the y axis. The gray solid line represents the residual.

IV.5 DISCUSSION

IV.5.1 PF Location and wind Stress

The mean location of the PF in Fig. 24 shows that the PF responds to different wind stresses. The local wind stress does affect frontal locations. However, this change in frontal location is relatively small compared to the effect of transport changes. In Chapter 3, the mean PF difference due to the transport changing can be as large as 300 km (Fig. 9). The maximum mean PF location difference occurs around I grid 50 in 6 hourly wind stress case. The difference is approximately 60 km. This implies the major impact on the frontal paths is the changing transport.

With the simple assumption that the surface elevation on the flanks of the PF represents the frontal shifting information, the surface elevation isoline moving means a shift in the PF. The PF locations response to the local wind stress are clear in these experiments. During most of the time periods, the direct response of the surface elevation to zonal component of wind stress changes is evident in the time series (Fig. 21). The coherency spectrum shows a significant (more than 90% confidence level) coherency of the wind stress and surface elevation at several time scales between 8 and 40 days. *Hughes et al.* [1999] stated that transport variations are dominated by barotropic mode between 10 days and 220 days. *Gille et al.* [2001] found that the ACC transport and the wind stress are coherent on time scales around 10-256 days. So in the model, the peaks at these frequencies are believed due to wind stress effects. In the smoothed wind stress, the oscillation in such periods is evident (Fig. 20). The phases corresponding to these peaks are negative most of the time. This states the wind stress leads the surface elevation changes. In *Gille et al.* [2001] and *Dong et al.* [2006] about the PF transport and the wind stress correlation, the transport variation usually slightly lags the wind stress.

At grid point (150,50), the coherency of the correlation between U wind stress and surface elevation is large, while the phase lag is positive. In the real Southern Ocean, the surface change (perturbation of SST) might lead the wind stress due to the air-sea interaction over seasonal time scales [*O'Neill et al.*, 2003]. However, in the model without the feedback of ocean to atmosphere, the positive phase lag might show the contribution of the local baroclinic activity instead the wind stress. Grid

point (150,50) lies farther north where the PF joins with the SAF in the model. Hence the strong frontal instabilities due to the topography and local baroclinic instabilities likely swamp the local wind stress as stated in *Hughes et al.* [1999].

Similar pattern of 500 m temperature tracked PF location and the surface PF states that the PF location correspond between the surface and subsurface layer. However, the surface PF location is usually to the south of the subsurface PF. This is consistent with the findings of *Dong et al.* [2006]. In their findings, the surface PF location is from the sea surface temperature gradient and the subsurface PF location is from the 200 m temperature in XBT data.

IV.5.2 PF variability and wind stress

The lack of the strong surface cooling in the model (negative) prevents the wind stress from producing a deep winter mixed layer. Therefore, the surface wind forcing mainly produces short term variations of the free surface (the barotropic response).

The standard deviation of the PF location does not show much difference between three surface forcing cases. Since the wind stress does correlate with the PF path, we would expect higher variability with stronger surface forcing if the PF location directly responds to the changing wind. From the PF location distribution in Fig. 19, this seems plausible. The PF with 6 hourly wind stress does have higher variability than the smooth wind stress case; however, the no wind situation gives a contradictory answer. The standard deviation of the variability due to different wind stress are relatively small compared to their mean values. This implies that factors other than the wind stress have more important effects, which might be the frontal baroclinic and barotropic instabilities or the topography induced eddies.

The wind stress in the model is local wind stress. The global wind stress is implied in the transport imposed along the western boundary of the model and does not change through the simulation. The global zonal wind stress accelerates the zonal transport of the PF [*Dong et al.*, 2006]. In case of the Southern Ocean westerlies might get stronger, such as with global warming. The stronger westerlies will impose larger transport on the PF from *Dong et al.* [2006]. From our model results in Chapter 3, the increased transport will shift the PF northward in the Drake Passage. However, out

of the Drake Passage, the PF shifting with the stronger westerlies may not follow this simple pattern without the special topographic constraints. The meridional shifting of the PF path corresponds to the meridional shifting of the wind fields [*Dong et al.*, 2006]. Though the transport in the PF increases with stronger westerlies, the PF out of the Drake Passage may not change according with the transport as it changes in Drake passage.

IV.5.3 Topographic effects

Topographic steering of the fronts is evident in the model. From the mean surface elevation, the SAF stays to the north and is aligned along the northern model wall. This is consistent with the SAF location in Chapter 3.

In the seamount region, the PF splits and merges with the SAF and the SACCF, respectively. Although splitting, each part of the PF has the same variability as the front that they join. So the variance of the PF location, if treated as one single front in this region, is very large. For each branch of the PF, the location variance is much smaller.

After a long simulation, the topographic steering of the fronts becomes more important than that in a feature model. In the seamount region, the PF deflects to the north when it encounters steep bottom topography. Conservation of potential vorticity $\frac{f+\zeta}{h}$ requires the northward excursion of the PF when bathymetry becomes shallower. In the real bathymetry of this region, the gap between the seamounts is wide enough that the PF can pass through. In the model, the gaps are smoothed out and the seamounts are deeper. In Fig. 19, two paths of the PF can be seen in this area. This splitting may not be realistic because the topography is changed by the smoothing procedure.

In the wind stress cases, the -5 cm and -10 cm isolines deflect northward past the ridge (Shackleton Fracture Zone, around $58°W, 59.7°S$). In the case without wind stress, the deflection is not so clear. The warm water from PF moves southward and is trapped there by the ridge. It then affects the path of the SACCF. The SACCF water is squeezed past the southern end of the Shackleton Ridge and then moves northeastward. In the time series (Fig. 20(c)(d)), the northward movement of an

eddy in the northeast of the ridge is evident at around day 1630. An interesting part in this area is that slightly different flow patterns in this area occur with different wind stress cases. Since the local wind stress affects the PF paths, the frequency and the strength of warm water intrusion from the PF might be affected also, and hence affect the flow structures here.

IV.5.4 Interpretation of form drag

In calculation of the form drag, the regions out of north and southern wall of Drake Passage are not included since an equal depth station could not be found for these areas. However, the majority of the flow (SAF and PF) stays on the north side of Drake Passage. So the complete effects of form drag on the ACC in Drake Passage could not be fully illustrated in this regional model. In a general discussion of the effect of Drake Passage on the ACC, the topographical effect is to squeeze the water into a narrow channel and hence increases the flow speed [*Rintoul et al.*, 2001; *Nowlin and Klinck*, 1986]. In the Southern Ocean form drag theory, the zonal direction form drag balances the wind stress [*Hughes*, 1997].

The form drag is on the order of $10^{-7} m/s^2$ (as in Fig. 27), while the wind stress (normalized by density and depth) is on the order of $10^{-8} m/s^2$. So the form drag in Drake Passage at least 10 times larger than the local wind stress. The x direction of the model domain (approximately the line length of form drag integration) is about 1000 km, which is approximately 1/20 of the circumpolar distance. So the Drake Passage form drag is on the same order of the total Southern Ocean wind stress along one latitudinal line. This tells us of the importance of Drake Passage in Southern Ocean dynamics. In numerical simulation of flow in the Southern Ocean, a realistic representation of topography is necessary to balance the wind stress.

Large standard deviations of the form drag term show that it changes with time, but the differences between the standard deviations found for different wind stress are small. The model reaches a dynamically steady state. The major circulation patterns do not change much from the wind stress changing, and neither does the bottom pressure. The variation of form drag at a fixed place is primarily from flow pattern changing due to the interior dynamics (the instabilities). This implies that the transport induced form drag is much larger than that from the local wind stress

and so the remote wind forcing in the whole Southern Ocean has more profound effects on the dynamics of the circulation in Drake Passage.

The analysis has elaborated how the wind stress affects the PF location and surface elevations. It seems reasonable to imagine that the frontal strength or location changing might affect total form drag if the PF moves. However, since the PF has more variability in flat bottom regions than in steeply sloped areas [*Moore et al.*, 1999; *Dong et al.*, 2006], the changing of form drag due to the frontal shifting from the wind stress might not be so evident.

IV.6 SUMMARY AND CONCLUSION

The study uses a regional ocean model in Drake Passage with different wind stress. Two kinds of wind stress, the 6 hourly wind stress interpolated from NCEP data and the monthly running mean filter smoothed wind stress, are used in contrasting experiments. With high frequency wind stress, the PF location is more variable; while with smooth wind stress, the PF is less variable.

The surface elevation to each side of PF changes with the wind forcing. The peak frequencies which the wind stress is correlated to the surface elevation above 95% confidence level are 8 and 30 days to the south with the wind stress leading the surface elevation. The peak frequencies to the north are 8, 15 and 40 days. The positive phase lag at some frequencies might be due to the contamination from the local baroclinic instabilities.

The mean 500 m temperature tracked PF location is consistent with mean surface PF location, while the surface PF tends to be south of the 500 m PF front. This difference between the surface and 500 m PF locations is modulated by the wind stress and the topography. With stronger wind stress, the difference will be reduced a bit because of the northward Ekman transport.

The mean form drag calculated in the model shows little changes with the different wind stress. The form drag in Drake Passage is calculated to be one order of magnitude larger than the local wind stress. The standard deviation of form drag with time is around $0.05 \sim 0.08 \times 10^{-6} m/s^2$, which changes less than $0.02 \times 10^{-6} m/s^2$ with different wind stress. The bottom stress can be neglected compared to these terms.

Form drag is primarily due to remote forcing (the transport variations) instead of the influence of the local wind stress.

CHAPTER V

CONCLUSIONS

These model results show a number of effects with different imposed volume transport. The variability of ACC fronts in Drake Passage is clearly related to the volume transport of the ACC. With large transport, the SAF and the PF are more stable. The PF and SAF spawn fewer eddies. The SAF, PF and SACCF shift northward with large transport while they remain to the south with smaller transport. With smaller transport, the SAF develops large meanders. The transport and the frontal variability reflect the competition between the frontal available potential energy and the kinetic energy. Consistency of input transport and the density fields is important for regional mesoscale circulation models.

In all the transport cases, the mean shifting distance of PF from its historical locations is from 50 km to 90 km, which brackets the estimate (70 km) by *Gille and Kelly* [1996]. The minimum shifting distance occurs at a transport of 135 Sv, which is consistent with the ISOS estimation to the total ACC transport of 134 Sv [*Whitworth*, 1983].

The SAF and SACCF are confined by northern and southern walls, respectively. The location of the PF is loosely controlled by the topography. After passing the seamounts in the central Drake Passage, the PF meanders strongly and becomes a wider flow.

The EPV is linearly correlated with the transport streamfunction between depths of 1500 meter to 2500 meter with a correlation of more than 0.9. Near-bottom flow has a weaker correlation between EPV and streamfunction. Near the surface, the correlation is weaker and even reverses sign.

The mean PF location changes with different wind stresses. With 6 hourly wind stress, the PF location is more variable, while with the smooth wind stress, the PF location is less variable.

The surface elevation on each side of the PF changes with the wind forcing. The peak frequencies at which the wind stress is correlated to the surface elevation, above

the 95% confidence level, are 8 and 30 days to the south with the wind stress change leading the surface elevation change. The peak frequencies to the north are 8, 15 and 40 days. The positive phase lag at some frequencies might be due to contamination from local baroclinic instabilities.

The mean 500 m temperature-tracked PF location is consistent with mean surface PF location, while the surface PF tends to be south of the 500 m PF front. This difference between the surface and 500 m PF locations is modulated by the wind stress and the topography, with a maximum mean difference of 90 km at the seamount region. With stronger wind stress, the difference will be reduced a bit because of the northward Ekman transport.

The mean form drag calculated in the model shows little change with the different wind stress. The form drag in Drake Passage is calculated to be one order of magnitude larger than the local wind stress. The standard deviation of form drag with time is around $0.05 \sim 0.08 * 10^{-6} m/s^2$, which changes less than $0.02 * 10^{-6} m/s^2$ with different wind stresses. The bottom stress can be neglected compared to these terms. Form drag is primarily due to remote forcing (the transport variations) instead of the influence of the local wind stress.

REFERENCES

Best, S. E., V. O. Ivchenko, K. J. Richards, R. D. Smith, and R. C. Malone (1999), Eddies in numerical models of the Antarctic Circumpolar Current and their influence on the mean flow, *J. Phys. Oceanogr.*, *29(3)*, 328–350.

Boyer, T., and S. Levitus (1998), Objective analysis of temperature and salinity for the world ocean on a 1/4 degree grid, *NOAA Atlas NESDIS.*

Cunningham, S. A., S. G. Alderson, B. A. King, and M. A. Brandon (2003), Transport and variability of the Antarctic Circumpolar Current in Drake Passage, *J. Geophys. Res.*, *108*, doi:10.1029/2001JC001147.

Dinniman, M. S., and J. M. Klinck (2004), Model study of circulation and cross shelf exchange on the west Antarctic Peninsula continental shelf, *Deep-Sea Res. II*, *50*, 3103–3120.

Dong, S., J. Sprintall, and S. T. Gille (2006), Location of the Polar Front from AMSR-E satellite sea surface temperature measurements, *J. Phys. Oceanogr.*, *36*, 2075–2089.

Dukowicz, J. K., and R. D. Smith (1994), Implicit free-surface method for the Bryan-Cox-Semtner ocean model, *J. Geophys. Res.*, *99(C4)*, 7991–8014.

Edwards, K. A., P. MacCready, J. N. Moum, G. Pawlak, J. Klymak, and A. Perlin (2004), Form Drag and mixing due to tidal flow past a sharp point, *J. Phys. Oceanogr.*, *34*, 1297–1312.

Gangopadhyay, A., A. R. Robinson, and H. G. Arango (1997), Circulation and dynamics of the western north Atlantic, I: Multiscale feature models, *J. Atmos. Oceanic Technol.*, *14(6)*, 1314–1332.

Gangopadhyay, A., A. Robinson, P. J. Haley, W. G. Leslie, C. Lozano, J. Bisagni, and Z. Yu (2002), Feature-oriented regional modeling and simulations (FORMS) in the Gulf of Maine and Georges Bank, *Cont. Shelf Res.*, *23*, 317–353.

Gent, P. R., W. G. Large, and F. O. Bryan (2001), What sets the mean transport through Drake Passage?, *J. Geophys. Res.*, *106(C2)*, 2693–2712.

Gill, A. E. (1982), *Atmosphere-Ocean Dynamics*, Academic Press, San Diego.

Gille, S. T. (1994), Mean sea surface height of the Antarctic Circumpolar Current from Geosat data: Method and application, *J. Geophys. Res., 99(C9)*, 18,255–18,273.

Gille, S. T. (1997), The Southern Ocean momentum balance: Evidence for topographic effects from numerical model output and altimeter data, *J. Phys. Oceanogr., 27*, 2219–2232.

Gille, S. T. (2005), Statistical characterization of zonal and meridonal ocean wind stress, *J. Atmos. Oceanic Technol., 22(9)*, 1353–1372.

Gille, S. T., and K. A. Kelly (1996), Scales of spatial and temporal variability in the Southern Ocean, *J. Geophys. Res., 101(C4)*, 8759–8773.

Gille, S. T., D. P. Stevens, R. T. Tokmakian, and K. J. Heywood (2001), Antarctic Circumpolar Current response to zonally-averaged winds, *J. Geophys. Res., 106*, 2743–2759.

Gnanadesikan, A., and R. W. Hallberg (2000), On the relationship of the circumpolar current to southern hemisphere winds in coarse-resolution ocean models, *J. Phys. Oceanogr., 30(8)*, 2013–2034.

Grose, T. J., J. A. Johnson, and G. R. Bigg (1995), A comparison between the FRAM results and observations in the Drake Passage, *Deep-Sea Res. Part I, 42*, 365–388.

Haidvogel, D., and A. Beckmann (1999), *Numerical ocean circulation modeling*, Imperial College Press, 318 pp.

Hedstrom, K. S. (2000), DRAFT Technical Manual for a Coupled Sea-Ice/Ocean Circulation Model (Version 2), *Tech. rep.*, Rutgers University.

Hofmann, E. E. (1985), The large-scale horizontal structure of the Antarctic Circumpolar Current from FGGE drifters, *J. Geophys. Res., 90*, 14,004–14,012.

Hofmann, E. E., and T. Whitworth (1985), A synoptic description of the flow at Drake Passage from year-long measurements, *J. Geophys. Res., 90(C4)*, 7177–7187.

Hughes, C. W. (1997), Comments on 'On the obscurantist physics of form drag in theorizing about the Circumpolar Current', *J. Phys. Oceanogr., 27(1)*, 209–210.

Hughes, C. W., and E. R. Ash (2001), Eddy forcing of the mean flow in the Southern Ocean, *J. Geophys. Res., 106(C2)*, 2713–2721.

Hughes, C. W., M. P. Meredith, , and K. J. Heywood (1999), Wind driven transport fluctuations through Drake Passage: A Southern Mode, *J. Phys. Oceanogr.*, *29*, 1971–1992.

Hughes, C. W., P. L. Woodworth, M. P. Meredith, and V. Stepanov (2003), Coherence of Antarctic sea levels, Southern Hemisphere Annular Mode, and flow through Drake Passage, *Geophys. Res. Lett.*, *30(9)*, 1464.

Inoue, M. (1985), Modal decomposition of the low-frequency currents and baroclinic instability at Drake Passage, *J. Phys. Oceanogr.*, *15*, 1157–1181.

Jackson, L., C. W. Hughes, and R. G. Williams (2006), Topographic control of basin and channel flows: The role of bottom pressure torques and friction, *J. Phys. Oceanogr.*, *36(9)*, 1786–1805.

Kamenkovich, I. (2005), The role of daily surface forcing in setting the temperature and mixed layer structure of the Southern Ocean, *J. Geophys. Res.*, *101(C7)*, doi:10.1029/2004JC002610.

Klinck, J. M. (1985), EOF analysis of central Drake Passage currents from DRAKE 79, *J. Phys. Oceanogr.*, *15*, 288–298.

Klinck, J. M., and E. E. Hofmann (1986), Deep-flow variability at Drake Passage, *J. Phys. Oceanogr.*, *16(7)*, 1281–1292.

Lima, I. D., D. B. Olson, and S. C. Doney (2002), Biological response to frontal dynamics and mesoscale variability in oligotrophic environments: Biological production and community structure, *J. Geophys. Res.*, *107(C8)*, 10.1029/2001JC000,864.

Maltrud, M. E., R. D. Smith, A. J. Semtner, and R. C. Malone (1998), Global eddy resolving ocean simulations driven by 1985-1995 atmospheric winds, *J. Geophys. Res.*, *103*, 30,825–20,853.

Marchesiello, P., J. C. McWilliams, and A. Shchepetkin (2001), Open boundary conditions for long-term integration of regional ocean models, *Ocean Modell.*, *3*, 1–20.

Mellor, G. L., L. Y. Oey, and T. Ezer (1998), Sigma coordinate pressure gradient errors and the seamount problem, *J. Atmos. Oceanic Technol.*, *15(5)*, 1122–1131.

Milliff, R., J. Morzel, D. Chelton, and M. Freilich (2004), Wind stress curl and wind stress divergence biases from rain effects on QSCAT surface wind retrievals, *J. Atmos. Oceanic Technol.*, *21*, 1216–1231.

Moore, J. K., M. R. Abbott, and J. G. Richman (1997), Variability in the location of the antarctic polar front (90-20w) from the satellite sea surface temperature data, *J. Geophys. Res.*, *102(C13)*, 27,825–27,833.

Moore, J. K., M. R. Abbott, and J. G. Richman (1999), Location and dynamics of the Antarctic Polar Front from satellite sea surface temperature data, *J. Geophys. Res.*, *104*, 3059–3073.

Munk, W., and E. Palmen (1951), Note on the dynamics of the Antarctic Circumpolar Current, *Tellus*, *3*, 53–55.

Nowlin, W. D., and M. Clifford (1982), The kinematic and thermohaline zonation of the Antarctic Circumpolar Current at Drake Passage, *J. Mar. Res.*, *40(Suppl)*, 481–507.

Nowlin, W. D., and J. M. Klinck (1986), The physics of the Antarctic Circumpolar Current, *Rev. Geophys. Space Phys.*, *24(3)*, 469–491.

O'Neill, L. W., D. B. Chelton, and S. K. Esbensen (2003), Observations of SST-induced perturbations of the wind stress field over the Southern Ocean on seasonal time scale, *J. Clim.*, *16*, 2340–2354.

Orsi, A. H., T. Whitworth, and W. D. Nowlin (1995), On the meridional extent and fronts of the Antarctic Circumpolar Current, *Deep-Sea Res.*, *42(5)*, 641–673.

Peterson, R. G. (1988), On the transport of the Antarctic Circumpolar Current through Drake Passage and its relation to the wind, *J. Geophys. Res.*, *93(C11)*, 13,993–14,004.

Peterson, R. G., W. D. Nowlin, and T. Whitworth (1982), Generation and evolution of a cyclonic ring at Drake Passage in early 1979, *J. Phys. Oceanogr.*, *12*, 712–719.

Rintoul, S., C. Hughes, and D. Olbers (2001), *Ocean Circulation and Climate, G. Siedler et al., Eds.*, vol. 77, Academic Press, San Diego, International Geophysics Series.

Sievers, H. A., and W. D. Nowlin (1984), The stratification and water masses at Drake Passage, *J. Geophys. Res., 89(C6)*, 10,489–10,514.

Sinha, B., and K. J. Richards (1999), Jet structure and scaling in Southern Ocean models, *J. Phys. Oceanogr., 29*, 1143–1155.

Smith, W. H. F., and D. T. Sandwell (1997), Global sea floor topography from satellite altimetry and ship depth soundings, *Science, 277(5334)*, 1956–1962.

Sokolov, S., and S. R. Rintoul (2002), Structure of Southern Ocean fronts at 140°E, *J. Mar. Sys., 37*, 151–184.

Sprintall, J. (2003), Seasonal to interannual upper-ocean variability in the Drake Passage, *J. Mar. Res., 61(1)*, 27–57.

Stommel, H. (1957), A survey of ocean current theory, *Deep-Sea Res., 4*, 149–184.

Sutyrin, G. G., I. Ginis, and F. A. Sergey (2001), Equilibration of baroclinic meanders and deep eddies in a Gulf Stream-type jet over a sloping bottom, *J. Phys. Oceanogr., 31*, 2049–2065.

Tanaka, Y. (2004), Development of super high-resolution atmospheric and oceanic general circulation models on quasi-uniform grids, *Annual Report of the Earth Simulator Center, Apr 2003-March 2004*, 13–16.

Tansley, C. E., and D. P. Marshall (2001), On the dynamics of wind-driven circumpolar currents, *J. Phys. Oceanogr., 31*, 3258–3273.

Thorpe, S. E., D. P. Stevens, and K. J. Heywood (2005), Comparison of two time-variant forced eddy-permitting global ocean circulation models with hydrography of the Scotia Sea, *Ocean Modell., 9*, 105–131.

Tomczak, M., and J. S. Godfrey (2003), *Regional Oceanography: An Introduction 2nd edn*, Daya Publishing House, Delhi, India.

Trenberth, K. E., J. G. Olson, and W. G. Large (1996), A global ocean wind stress climatology based on ECMWF analyses, *Tech. Rep. NCAR/TN-338+STR*, NCAR.

Wang, Z., A. C. Bovik, H. R. Sheikh, and E. P. Simoncelli (2004), Image quality assessment: From error visibility to structural similarity, *IEEE Trans. on Image Process., 13(4)*, 600–612.

Warren, B., J. H. LaCasce, and P. E. Robbins (1996), On the obscurantist physics of "Form Drag" in theorizing about the Circumpolar Current, *J. Phys. Oceanogr.*, *26*, 2297–2301.

Webb, D., de Cuevas, B., and the FRAM Group (1991), An eddy-resolving model of the Southern Ocean, *Eos Trans. AGU, 72(15)*, 169–174.

Weijer, W., and S. T. Gille (2005), Adjustment of the Southern Ocean to wind forcing on synoptic time scales, *J. Phys. Oceanogr.*, *35*, 2076–2089.

Well, R., W. Roether, and D. P. Stevens (2003), An additional deep-water mass in Drake Passage as revealed by ^{3}He data, *Deep-Sea Res. I*, *50*, 1079–1098.

Whitworth, T. (1980), Zonation and geostrophic flow of the Antarctic Circumpolar Current at Drake Passage, *Deep-Sea Res.*, *27A*, 497–507.

Whitworth, T. (1983), Monitoring the transport of the Antarctic Circumpolar Current at Drake Passage, *J. Phys. Oceanogr.*, *13*, 2045–2057.

Whitworth, T., and R. G. Peterson (1985), Volume transport of the Antarctic Circumpolar Current from bottom pressure measurements, *J. Phys. Oceanogr.*, *15*, 810–816.

VITA

Bin Zhang
Department of Ocean, Earth and Atmospheric Sciences
Old Dominion University
Norfolk, VA 23529

1. Education

   1999-Present, Ph.D, Center for Coastal Physical Oceanography, Old Dominion University

   1996-1999, M.S, Physical Oceanography, Institute of Oceanology of Chinese Academy of Sciences

   1991-1996, B.S, Geophysics, University of Science and Technology of China

2. Research Experience

   Research Assistant, 1999-2006, Center for Coastal Physical Oceanography, Old Dominion University

   Research Assistant, 1996-1999, Physical oceanography Department, the Oceanology Institute of Chinese Academy of Sciences

3. Publications

   Freshwater transport estimate for the Gulf of Alaska, Bin Zhang and Thomas Royer, In revision to Geophysical Research Letters

   The effects of Antarctic Circumpolar Current transport on the frontal variability in Drake Passage, Bin Zhang and John M Klinck, in review, Dynamics of Atmosphere and Oceans

4. Reports

   The General and Extreme Hydrology Conditions in the area of Ocean Oil Platforms in Bohai Sea, South China Sea and East China Sea. Guohong Fang, Bin Zhang et al., 1997-1999

Typeset using LaTeX.